DESIGN AND VALIDATION OF A COMBUSTION TEST RIG FOR AIRBREATHING ROCKET PROPULSION STUDIES

A THESIS SUBMITTED TO
THE GRADUATE SCHOOL OF NATURAL AND APPLIED SCIENCES
OF
MIDDLE EAST TECHNICAL UNIVERSITY

BY

EMRE SONGÜR

IN PARTIAL FULFILLMENT OF THE REQUIREMENTS
FOR
THE DEGREE OF MASTER OF SCIENCE
IN
MECHANICAL ENGINEERING

DECEMBER 2010

Approval of the thesis:

DESIGN AND VALIDATION OF A COMBUSTION TEST RIG
FOR AIRBREATHING ROCKET PROPULSION STUDIES

submitted by **EMRE SONGÜR**, in partial fulfillment of the requirements for the degree of **Master of Science in Mechanical Engineering Department, Middle East Technical University** by,

Prof. Dr. Canan ÖZGEN ______________________
Dean, **Graduate School of Natural and Applied Sciences**

Prof. Dr. Süha ORAL ______________________
Head of Department, **Mechanical Engineering**

Assoc. Prof. Dr. Abdullah ULAS ______________________
Supervisor, **Mechanical Engineering Dept., METU**

Dr. K.Atılgan TOKER ______________________
Co-supervisor, **Roketsan A.S.**

Examining Committee Members:

Prof. Dr. Kahraman ALBAYRAK ______________________
Mechanical Engineering Dept., METU

Assoc. Prof. Dr. Abdullah ULAS ______________________
Mechanical Engineering Dept., METU

Prof. Dr. Hüseyin VURAL ______________________
Mechanical Engineering Dept., METU

Prof. Dr. Nafiz ALEMDAROĞLU ______________________
Aeronautical Engineering Dept. METU.

Dr. K.Atılgan TOKER ______________________
Roketsan A.S.

Date: December 17, 2010

I hereby declare that all information in this document has been obtained and presented in accordance with academic rules and ethical conduct. I also declare that, as required by these rules and conduct, I have fully cited and referenced all material and results that are not original to this work.

Name, Last name : Emre SONGÜR

Signature :

ABSTRACT

DESIGN AND VALIDATION OF A COMBUSTION TEST RIG
FOR AIR BREATHING ROCKET PROPULSION STUDIES

Songür, Emre
M. Sc., Department of Mechanical Engineering
Supervisor: Assoc. Prof. Dr. Abdullah Ulas
Co-Supervisor: Dr. K.Atılgan Toker

December 2010, 103 pages

The aim of this thesis is to develop a general purpose combustion test rig for air-breathing propulsion. The test rig is capable of examining flame structures and combustion efficiencies of different fuels and air-fuel mixtures in air breathing rocket engines.

During the design of the test rig, CFD simulations of the reactive flows are performed. Design of Experiments methodology is employed to compare the effect of combustor geometry and air to fuel ratio on combustion efficiency. Mechanical design of the test rig is carried out to achieve high number of tests at elevated temperatures. High temperature instrumentation system is designed for gathering measurements. Infrared thermography, thermocouples with platinum, tungsten and rhenium materials for combustor temperature measurements, piezoresistive pressure sensors with high frequency response for oscillating pressure measurements and high speed cameras for flow visualization are used. A data acquisition software is also developed for the test rig.

After design, manufacturing and assembly operations are completed; system check-out is performed for validation of the test rig design. Five reactive flow experiments are performed at different fuel to air ratios. Functionality of the test rig is verified with the first reactive flow experiment. Combustion efficiencies are determined in three experiments. Thermocouple dynamic behavior is investigated by the fifth reactive flow experiment.

It is observed that increasing fuel to air ratio and combustor temperature leads to combustion efficiency increase. It is also verified that the designed test rig achieves the aim of investigating flame structure and combustion efficiency.

Key-words: Air-breathing Propulsion, Combustion Testing, High Temperature Instrumentation.

ÖZ

HAVA SOLUMALI ROKET MOTORU ÇALIŞMALARINA YÖNELİK BİR YANMA TEST DÜZENEĞİNİN TASARIMI VE DOĞRULANMASI

Songür, Emre
Yüksek Lisans, Makina Mühendisliği Bölümü
Tez Yöneticisi: Doç. Dr. Abdullah Ulaş
Ortak Tez Yöneticisi: Dr. K.Atılgan Toker

Aralık 2010, 103 sayfa

Bu tez kapsamında,hava solumalı roket çalışmaları için kullanılabilecek genel maksatlı bir yanma test düzeneği geliştirilmiştir. Test düzeneği farklı yakıtların ve farklı yakıt hava karışım oranlarının, yanma verimi ve alev yapısına etkisini inclemek için kullanılmaktadır. Test düzeneğinin iç balistik tasarımı sırasında; yanma odasının kesit alanının, farklı yakıt ve hava oranlarının akış alanındaki değişimlerden en az etkilenecek şekilde incelenebilecek kadar geniş olduğu HAD simülasyonları ile görülmüştür. Akış alanını etkileyen geometrik parametrelerin ve yakıt hava oranının etkisinin karşılaştırılması için deney tasarımı yöntemleri kullanılmıştır. Test düzeneğinin mekanik tasarımı, yüksek sıcaklıkta çok sayıda testin, en az bakım ihtiyacı ile yapılabileceği şekilde gerçekleştirilmiştir. Yüksek sıcaklık ölçüm sistemleri tasarlanarak uygun ekipmanlar kullanılmıştır. Sıcaklık ölçümleri için kızıl ötesi termografi; platin, tungsten ve renyum içeren ısıl çiftler, yüksek sıcaklıklarda basınç osilasyonlarının ölçülmesi için piezoresistif basınç sensörleri ve akış görüntülenmesi için yüksek hızlı kameralar kullanılmıştır. Veri toplama sisteminin kullanılması için de bir yazılım hazırlanmıştır.

Soğuk akış ve yanma testleri, test düzeneği kullanılarak gerçekleştirilmiştir. Dört yanma testi yakıtça zengin ve oksitleyicisi zengin farklı yakıt ve hava oranlarında gerçekleştirilmiştir. Bir beşinci test ise ısıl çiftlerin dinamik davranışını incelemek için yapılmıştır. Yakıt hava oranının artması ve yükselen yanma odası sıcaklıkları ile verim artışı olduğu gözlenmiştir. Yanma veriminin hesaplanması için gerekli ölçümler alınmıştır.

Tasarlanan test düzeneğinin yeteneklerinin, yanma incelenmesi ve yanma veriminin tespiti için gerekli ölçümlerin alınmasına izin verdiği görülmüştür. Test düzeneği farklı yakıt ve yakıt ile hava karışım oranlarının, hava solumalı roketler içerisindeki yanmasının incelenmesi için kullanılabilecektir.

Anahtar Kelimeler: Hava Solumalı İtki, Yanma Testi, Yüksek Sıcaklık Enstrumantasyonu.

Babama,

ACKNOWLEDGEMENT

I would like to express my deepest thanks and gratitude to Assoc. Prof. Dr. Abdullah ULAS for his supervision and constant guidance through this study.

I would like to thank to my co-supervisor Dr. Kemal Atılgan TOKER, for his advises and to Dr. Tuğrul TINAZTEPE for his support. Also special thanks to Prof. Dr. Sermet ANAGÜN as he taught me the fundamentals of the design of experiments approach, very clearly in a very brief time.

I would like to express my sincere appreciation to my colleague Utku OLGUN for crucial advises on CFD modeling of the problem.

I would also like to thank to my friends Mehmet ÇAVUŞ, Alkım ARIN, Elif ALP, Sinan KAPOĞLU and Hasan HIZLI for their friendship and help.

Special thanks go to my wife Özge and my entire family for always being there for me and giving me the motivation.

This thesis is dedicated to my family, without them nothing would have been made.

TABLE OF CONTENTS

LIST OF TABLES

TABLES

LIST OF FIGURES

FIGURES

LIST OF SYMBOLS

A_e	Nozzle exit area
A_{th}	Nozzle throat area
a	Speed of sound
A/F	Air to fuel ratio
C*	Characteristic velocity
C	Constant
C_d	Discharge coefficient
c_p	Specific heat
D_t	Nozzle throat diameter
F	Thrust
$F_{h,j}$	Diffusional energy flux at x_j
$F_{m,j}$	Diffusional flux at x_j
F/A	Fuel to air ratio
F_H	Helmholtz frequency in a cavity
g_0	Gravitational acceleration at sea level
h	Specific Enthalpy
h_f	Adiabatic combustion enthalpy of fuel
H_m	Enthalpy of formation of m
I_{sp}	Specific impulse
k	Turbulent kinetic energy
L	Length
$\dot{m}$	Mass flow rate
M_e	Exit Mach number
P	Pressure
P_{amb}	Ambient pressure
P_c	Chamber pressure

P_e	Nozzle exit pressure
R	Gas constant
$S_{i,j}$	Mean strain
s_m	Mass source
s_i	Momentum source
s_h	Energy source
t	Time
T	Temperature
u_i	Fluid velocity component at x_i
v_e	Velocity at nozzle exit
x_i	Cartesian coordinate
V	Volume
Y_m	Mass fraction of m in a mixture

Greek Symbols:

ρ	density
γ	specific heat ratio
∂	partial derivative operator
η	efficiency
τ_{ij}	stress tensor components
ε	turbulence dissipation rate
μ_t	turbulent viscosity
λ	wavelength of light

Subscripts:

f	fuel
a	air
t	total

amb	ambient
exp	experimental
the	theoretical
th	thermal

Abbreviations:

PLIF	Planar Laser Induced Fluorescence
LDV	Laser Doppler Velocimetry
PIV	Particle Image Velocimetry
IR	Infrared
LWIR	Long Wave Infrared
DOE	Design of Experiments
DOF	Degree of Freedom

CHAPTER 1

INTRODUCTION

In this thesis, a combustion test rig for investigation of flames and combustion efficiencies of different fuels and different air to fuel ratios in air breathing rocket combustors is developed.

Solid and liquid propellant rockets contain stoichiometric amount of fuel and oxidizer. In contrast to rocket engines, air breathing rockets do not carry oxidizer or carry less than stoichiometric amount as they use air as oxidant in their combustors. Therefore air breathing rockets need less amount of propellant to be carried, which makes them either lighter or able to travel greater distances. Despite having advantages over other rocket propulsion systems, air breathing rockets are not widely used in operational systems due to the technological challenges. One of the technological challenges in air breathing propulsion is to design efficient, reliable and robust combustion chambers. Moreover performance of air breathing rockets is strongly sensitive to the performance of their combustion chambers. Therefore, large amount of experimental data on combustion of fuels with air is needed. Fundamentals of air breathing rocket combustion are investigated by test rigs with sub-scale combustors.

The combustion process involved in air breathing rockets has highly complex turbulent flow, mixing and thermochemistry problems. Thus, performance of the combustion chambers can be determined by full scale tests with final configuration which are very costly. Detailed CFD simulations also need powerful computers and very long run times. Furthermore, most of the time CFD simulations can not predict the real performance.

However a large amount of tests are needed during the development of fundamental concepts. Hence, simplified and scaled combustors are needed for fundamental experimental studies in combusting chambers. In this study, a test rig with a scaled combustor is designed, manufactured and its design is verified conducting experiments.

1.1 SCOPE OF THE THESIS

The purpose of this study is to develop a combustion test rig for air breathing rocket combustion studies. A detailed literature survey on previous test rigs and experimental studies is performed. Experimental approach to the combustor problem is investigated and measurement techniques used in air breathing rocket combustors are determined.

Design of the test rig is performed in this study. Conceptual design is made to satisfy test requirements. Using CFD as a tool, internal ballistic design was made to define test rig combustor geometry and probe locations. First aim of the CFD simulations is to ensure if the cross section area of the sub-scale combustor is large enough to investigate different air to fuel ratios with minor effect from flow field. Design of Experiments (DOE) methodology is used to compare the effect of combustor geometry and air to fuel ratio on combustion efficiency. Second aim was to determine suitable probe locations. Flow inside the combustor is very complex hence proper probe locations are selected at positions where flow velocities are near stagnation and static temperature is close to combustor exit temperature. Mechanical design of the test rig was conducted for a low maintenance operation of the rig. Instrumentation system design of the test rig is done for temperature and pressure measurements from high temperature gas and flow visualization.

Experiments at different fuel to air ratios are conducted. Hot gas products of fuel rich combustion of a hydrocarbon fuel is used in the experiments. The hot gas fuel was composed of hydrogen, carbon monoxide and other inert products. Temperature, pressure and high speed camera data is gathered. These data is used for efficiency calculation and investigation of the physics of the problem.

Hence a test rig which is able to perform experiments to compare combustion characteristics and combustion efficiency of different fuels and fuel to air mixture ratios by making temperature and pressure measurements is developed. By design verification experiments, it is investigated if the test rig is capable to satisfy this requirement.

1.2 CONTENTS OF THE THESIS REPORT

Literature survey, properties of previous sub-scale combustors and studies done with them are presented in this chapter.
In Chapter 2, a background on fundamentals of air breathing engines is given.
Chapter 3 contains the detailed description of the combustion test rig design. Conceptual design, mechanical design, internal ballistic design of the test rig and instrumentation system design are presented in this chapter. Experimental cases and their results are presented in Chapter 4. Discussion and conclusions are given in Chapter 5. Sample Analysis of Variance (ANOVA) calculation used in Design of Experiments are given in APPENDIX A and Data Acquisition Software block diagram is given in APPENDIX B.

1.3 LITERATURE SURVEY

Sub scaled combustors for air breathing rocket combustion chamber development are being used since late 1960's.

In 1969, Schadow used a square crossection subscale combustor with quartz windows to investigate mixing and burning between subsonic air and supersonic particle laden fuel. Both quantitative T,P measurements and qualitative flow field examination by a high speed camera were made [1]. In 1973, Schadow investigated effects of combustion chamber pressure and air to fuel ratio on combustion efficiency by using the subscale combustor [2]. Abbot conducted experiments with different fuels, combustion chamber pressures and air to fuel ratios in 1974. Water cooled probes were used for detailed examination of the flame [3].

In 1975, a metal and metal oxide particle seeding system was used by Schadow in subscale combustor tests [4].

The experimental setup in the Naval Weapons Center USA has been used in early works in air breathing engine combustor development. It has a square crossectioned combustor. Fuel rich gas is fed into a concentric airstream. Air flow can be chocked either in the nozzle after the combustor or in the upstream. Hence both constant air flow rate and combustor pressures can be achieved separately.

Experiments were conducted to investigate the effects of fuel to air ratio, combustor pressure and fuel compositions on mixing and combustion. Temperature and pressure measurements were made by high temperature thermocouples and pressure probes. Quartz windows on the combustor also allowed flow visualization. Temperature distribution was estimated from color distribution in images which were recorded by cameras. [1], [2],[3].

18 different experiments were made by Schadow [1]. 16 experiments were made by using air at ambient temperature which was 280 K. Two of the experiments was made with heated air at 650 K. Air to fuel ratios were varied from 3.6 to 15.5. Fuel temperatures were between 750K and 2720 K.

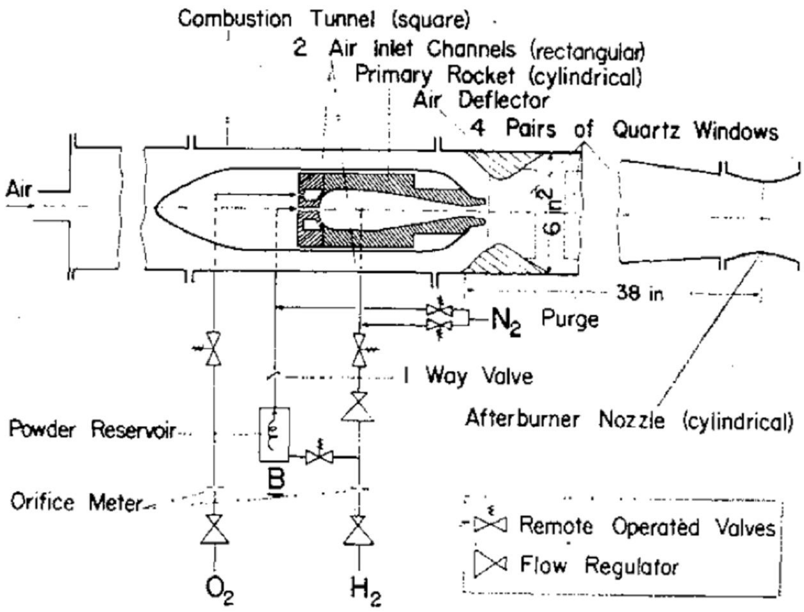

Figure 1-1 Combustion Test Rig and Propellant Feed System [1]

Temperature measurements from combustor were done. Also high speed camera images were used for qualitative investigation of temperature distribution in the flow field. A sketch of two different air to fuel ratio cases (Test No. 1: 6.7 and Test no. 16: 15.5) is given in Figure 1-2. Black parts are colder regions before ignition.

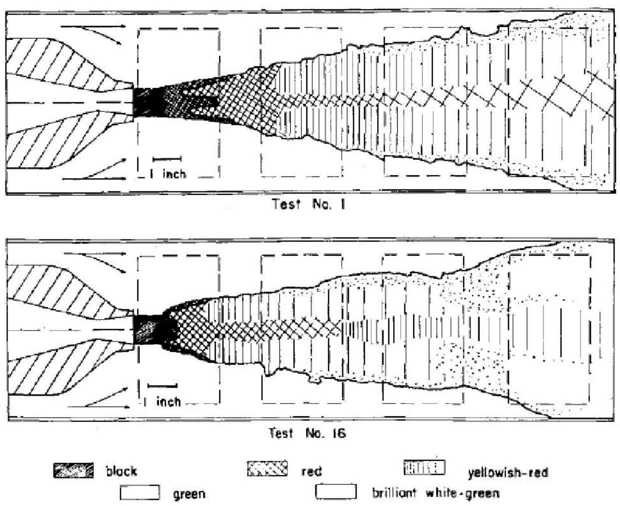

Figure 1-2 Combustion Behavior at Different Air to Fuel Ratios [1]

Higher temperatures and efficiencies are reported in the case of greater air to fuel ratio as the air flow was more turbulent. However, Shadow also stated that same nozzle was used in both cases so increased pressure may be another reason of efficiency increase. Also an increase in C* efficiency due to the higher fuel temperatures were reported. C* efficiency rise with increasing fuel temperature is given in Figure 1-3.

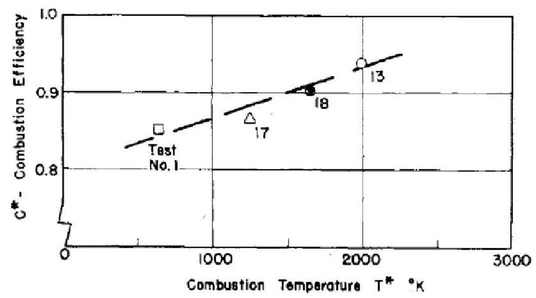

Figure 1-3 C* Efficiency of Tests No 1, 17 18 and 13 [1]

Abbot made some improvements to the test rig. A sketch is given in Figure 1-4 [3]. Gas chromatography and particle sampling were made for better efficiency investigation.

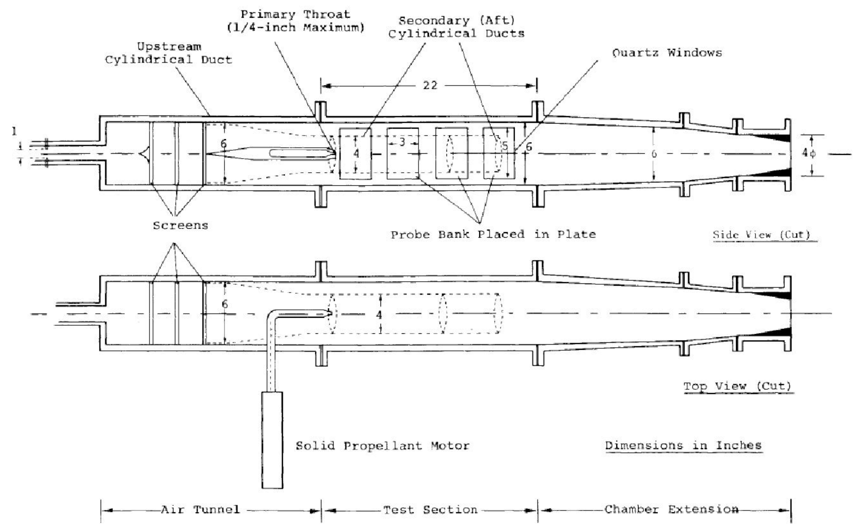

Figure 1-4 Combustion Test Rig [3]

Water cooled gas and particle sampling probes shown in Figure 1-5 were used in four experiments with 190, 200, 275 and 57 psi combustor pressures. Better particle combustion is reported at higher pressures by examining the collected particles.

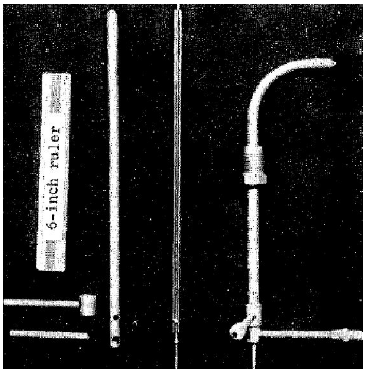

Figure 1-5 Water Cooled Sampling Probe

In 1983 Clark used an experimental combustor to investigate pressure oscillations in combustors burning liquid fuel [5]. In 1986, Crump investigated longitudinal combustion instabilities by using a subscale combustor. Detailed pressure measurements, including both amplitude and phase were made in ten locations [6].

This test rig was used for investigation of longitudinal combustion instabilities in liquid fuel combustion. A dumped combustor was used. Detailed pressure measurements can be done on different locations. Both the amplitude and the phase of the pressure could be measured.

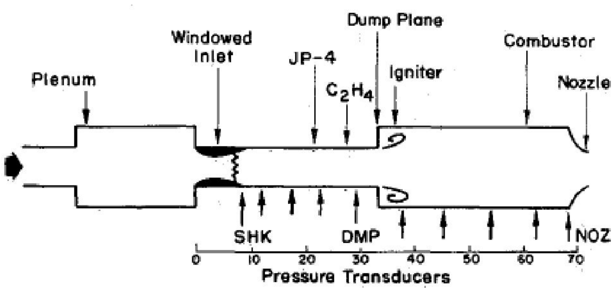

Figure 1-6 Combustion Stability Test Rig [6]

Pressure fluctuations from 170 to 650 Hz were reported both in JP-4 and ethylene combustion. Effect of the combustor geometry on oscillations was studied. Effect of inlet length had minor effect. In contrast, combustor geometry had a direct effect on the first mode of the longitudinal vibrations as given in Figure 1-7.

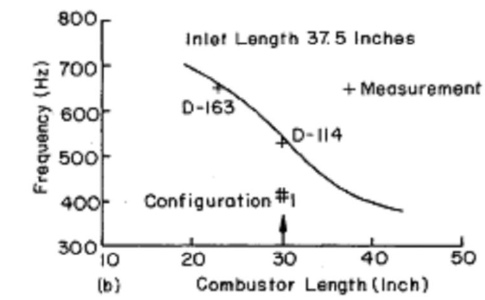

Figure 1-7 Longitudinal Pressure Oscillations [6]

In 1988 Liou used a model combustor made from plexiglas to examine flow field inside the air breathing rocket combustor. Velocity measurements were made by Laser Doppler Velocimetry [7].

A plexiglass side dump combustor with two air inlets was used for cold flow tests in National Tsing Hua University. Optical measurement methods like LDV have been used as the combustor is transparent. Velocity profiles, position of jet impinging points and turbulent properties of the flow were investigated by detailed velocity measurements. [7]

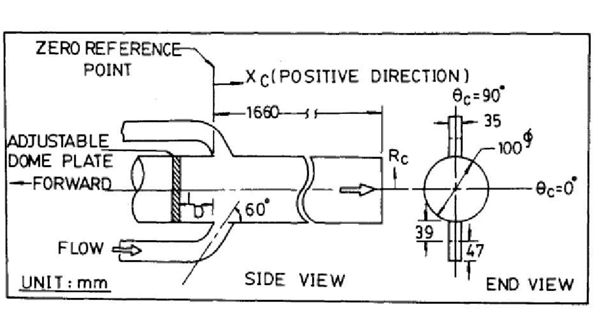

Figure 1-8 Cold Flow Combustor Geometry [7]

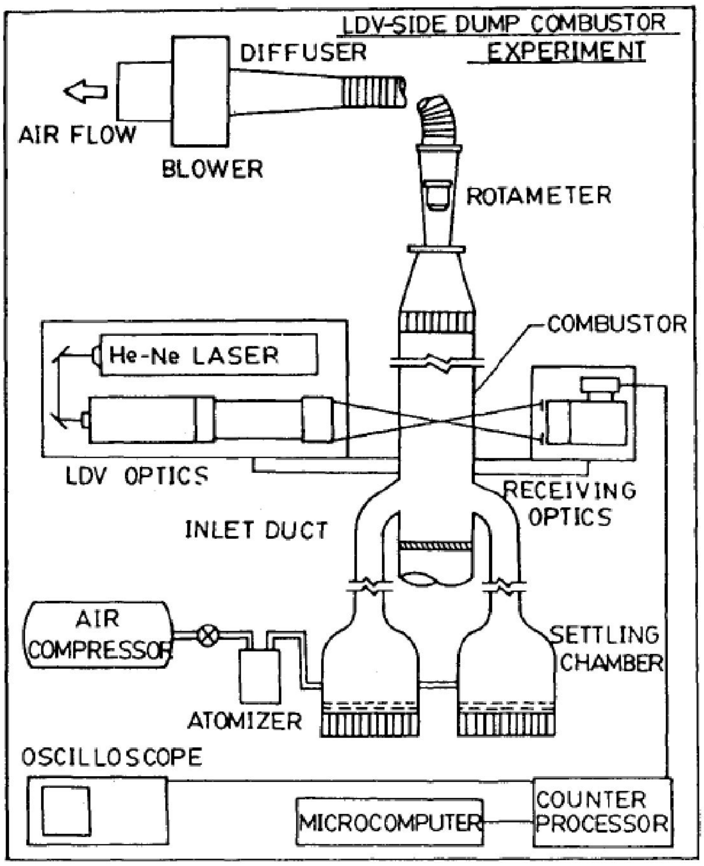

Figure 1-9 Cold Flow Combustor Test Rig [7]

Cherng made numerical simulation of a ducted rocket combustor model. Air inlet angles and dome height was varied. Also cold flow tests were made by using a model combustor with windows and Schilieren images were taken [8].

Stull and Vanka studied liquid fuel combustion in a circular crossectioned combustor. Experiments were conducted with different air inlet angles and dome heights [9],[10]. Stull used an experimental combustor where air inlet angles and dome height (distance between fuel injection point and air inlet) were variable. Pressure distribution on the combustor wall was measured to investigate the changes in the flow field with different air inlet angles and dome heights.

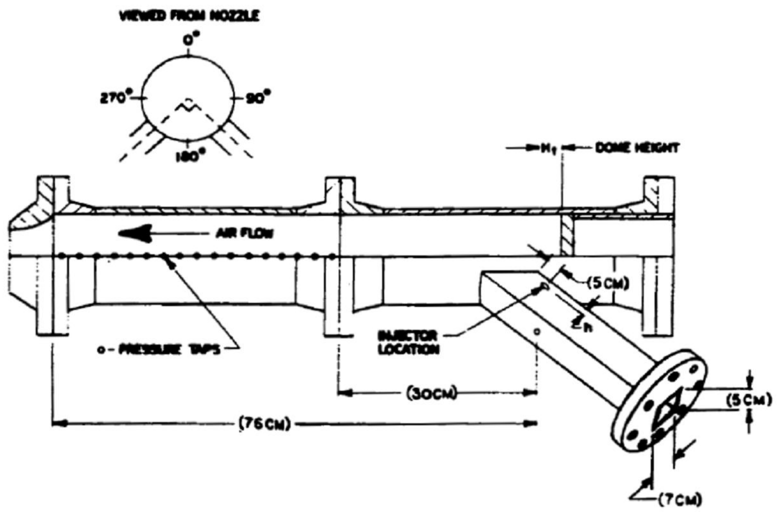

Figure 1-10 Variable Geometry Combustor of Stul *et al.* [9]

Air inlet crossection was 50 mm by 70 mm with the long dimension aligned to the main axis. Angle between the air inlets was 90º. Diameter of the combustor was 150 mm. Air inlet angles of 30°, 45°, and 60° from the horizontal were studied. Air inlet speed was 0.5 Mach. Dome height was varied from 25 to 150 mm. Air inlet angle had little effect on combustion efficiency. Optimum value was 60°. Combustion efficiency was more sensitive to dome height. 50 mm was the optimum value. It was also observed that an eccentric fuel injection, increased combustion efficiency [9].

Schadow used nozzles with elliptic crossection to enhance mixing in the subscale combustor in 1987 and 1988. Both non reacting and reacting tests were made [11], [12]. Gutmark continued this work by using square and triangular crossectioned nozzles in 1991 [13].

In 1990 Schadow studied the effect of enhancement of fine-scale turbulence for improving combustion efficiency in the sub scale combustor. PLIF was used for flow visualization of OH radicals in the reacting flow [14]. Schadow also used another sub-scaled combustor with multi-step dumps to reduce combustion instabilities [15].

Effect of fuel injector crossection on jet structure and mixing was investigated by both cold flow and reacting flow tests. Rectangular, triangular and elliptical injector crossections were used. Also dumped stages were used in injectors. Mixing studies were done by cold flow experiments where nitrogen and air was used. Combustion experiments were done by using a hot fuel from a gas generator. [11][14]

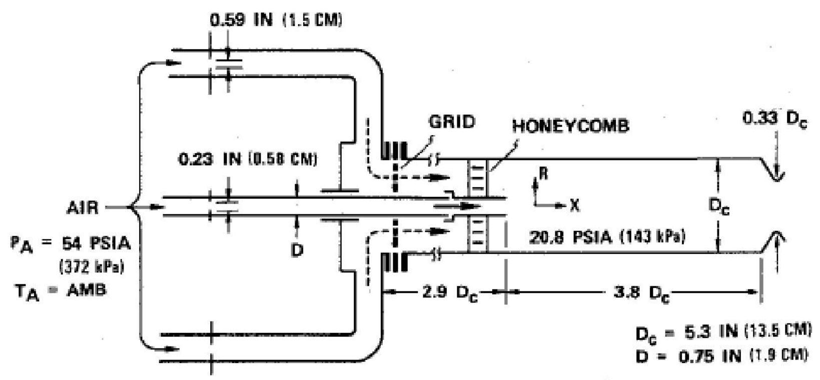

Figure 1-11 Injector Geometry Cold Flow Test Rig [11]

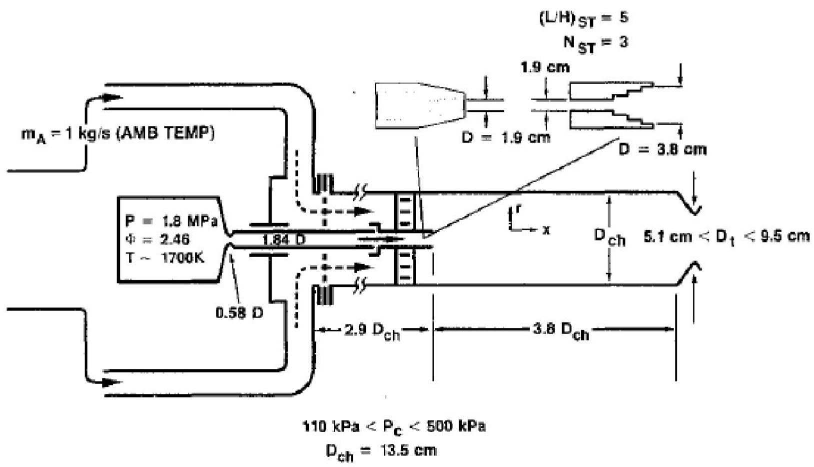

Figure 1-12 1-13 Injector Geometry Reacting Flow Test Rig [14]

Shadow used a fuel injector with an elliptical crossection. Different aspect ratios were studied. During the combustion tests, most significant spread was in the elliptical jet with the 3:1 ratio. Both 2:1 and 3.5:1 jets had lower spreading rates in the minor axis plane than the 3:1 and the circular jet [11].

In another study of Schadow, a multi step injector given in Figure 1-12. This resulted in an increase of fine scale turbulence of fuel jet. Higher temperatures and shorter flame length was observed in combustion experiment. A comparison of axial temperature distribution is given in Figure 1-14.

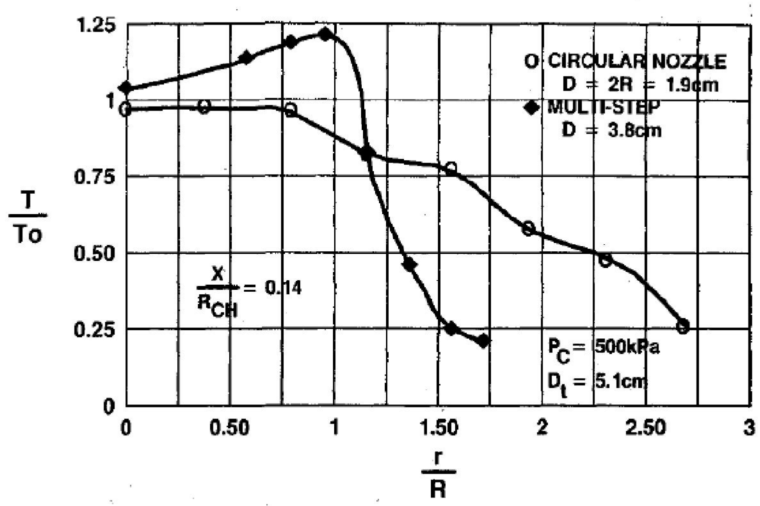

Figure 1-14 Axial Temperature Distribution of Circular and Multistep Injector

In 1991, Ajdari used an infrared camera for thermal imaging of combustion in ducted rockets [16]. Albagli used an experimental combustor with particle seeding system. LDV was used for velocity measurements. Sampling probes were used for gas composition analysis [17]. This test rig was used for cold flow tests. Mixing of coaxial flows was investigated. Test results were also used for validation of the numerical simulations of the flow. Pressure distribution over the walls, tracer gas concentration, and two-phase velocity measurements were made. Air and fuel flow was choked at the upstream of the combustor so different mass flow rates of air and fuel can be achieved separately. Combustor was made from glass and transparent PVC to allow LDV measurements. Cold flow tests were made at ambient temperature and pressure conditions which were 300K and 100 kPa respectively. Flow velocities at different positions were measured by LDV.

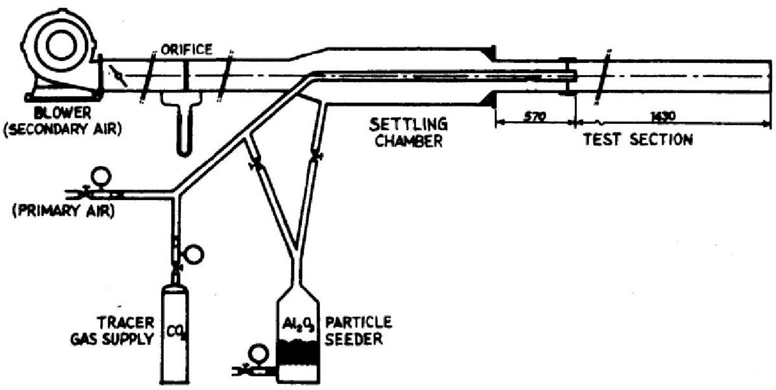

Figure 1-15 Ramcombustor Test Rig for Mixing Investigation [17]

Dijkstra, in 1991, made experiments which were focused on how the shape of the injectors affects the combustion efficiency in a subscale combustor [18]. In 2004, Stowe used a model combustor and conducted experiments by varying the injector type, the dome height and air to fuel ratio.

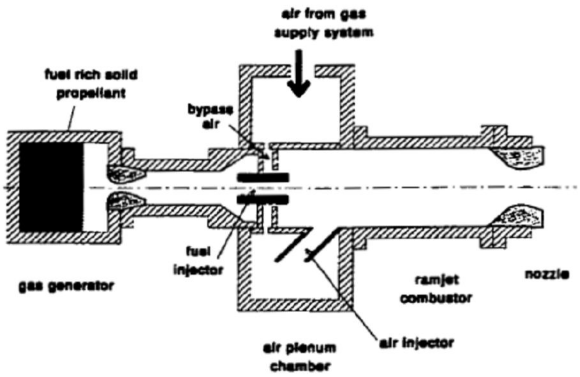

Figure 1-16 Combustor with Solid Propellant Gas Generator [19]

A simulated fuel which is obtained by ethylene combustion was used to simulate solid fuel gas generator products [20]. Both simulated fuel and solid propellant gas generator can be used in this experimental combustor. Simulated fuel is generated by fuel rich combustion of C_2H_4. The combustor is cylindrical and has two air inlets. Different fuel injector positions, fuel injector crossection areas, fuel to air ratios, gas generator and combustor pressures can be investigated. This combustor was also used to verify numeric simulations. [20],[19].

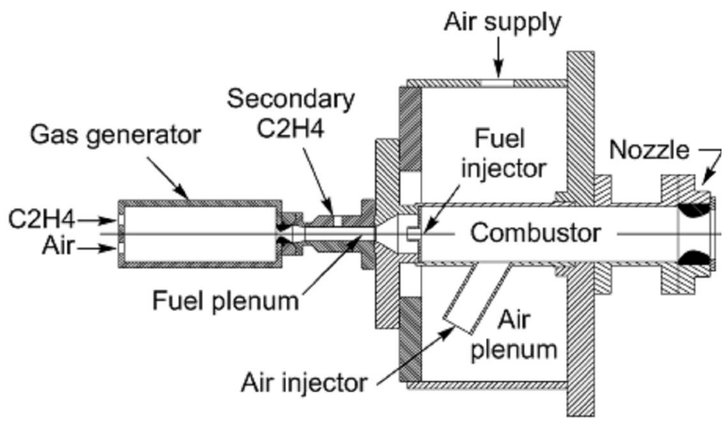

Figure 1-17 Combustor with Simulated Fuel Gas Generator [20]

Dome heights of 57 mm and 100 mm were used in this study. Different fuel injectors and fuel to air ratios were used. Air inlet angles were not varied. One stream and two stream PDF modeling of the reactive flow was done by using FLUENT.

30 experiments and 60 CFD simulations was made by Stowe [20]. However CFD simulation results based on one and two stream probability density function (PDF) could not have been correlated to experimental results as can be seen from Figure 1-18.

Reason for this was suggested as the high frequency pressure oscillations in the combustor which could not be simulated by CFD.

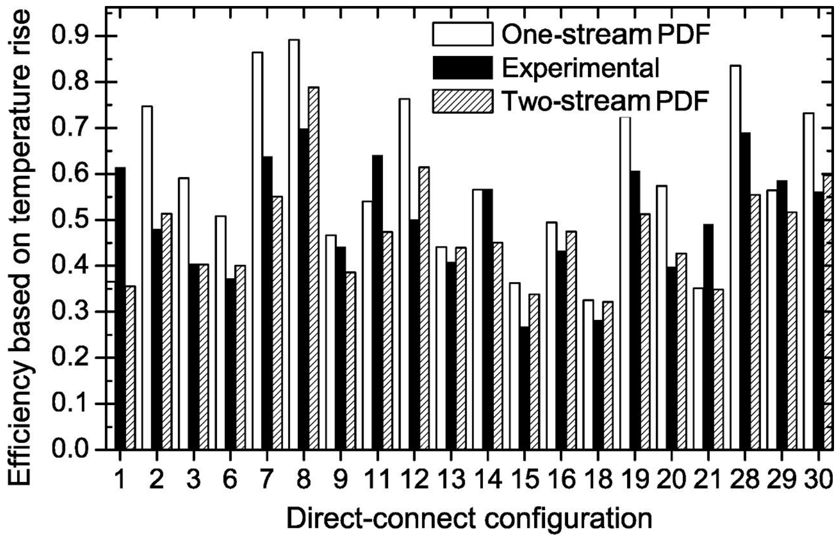

Figure 1-18 CFD and Experiment Results [20]

In 1995 Brophy used an optically accessible stainless steel model combustor with four air inlets for flow visualization [21].

This test rig had a for air inlet combustor. Different injector, fuel to air ratios and fuel inlet angle combinations were investigated at cold gas and reacting flow tests. Combustor was made from stainless steel and had windows for optical access.

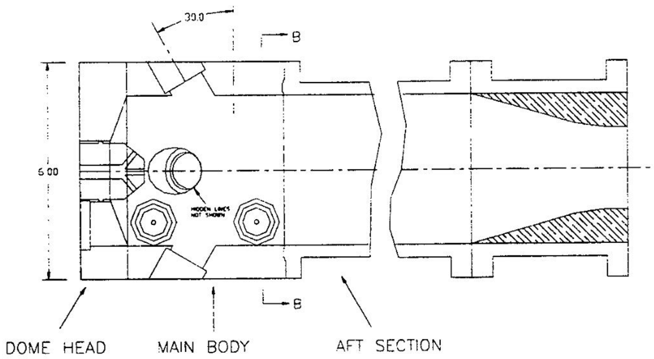

Figure 1-19 Four Air Inlet Combustor [21]

Fuel dispersions and vortex structures were studied at three different air inlet angles which were 90°, 60° and 45°. Flow visualization sketches are given Figure 1-20. Vortices in 60º configurations provide better fuel and air mixing in dome region [21].

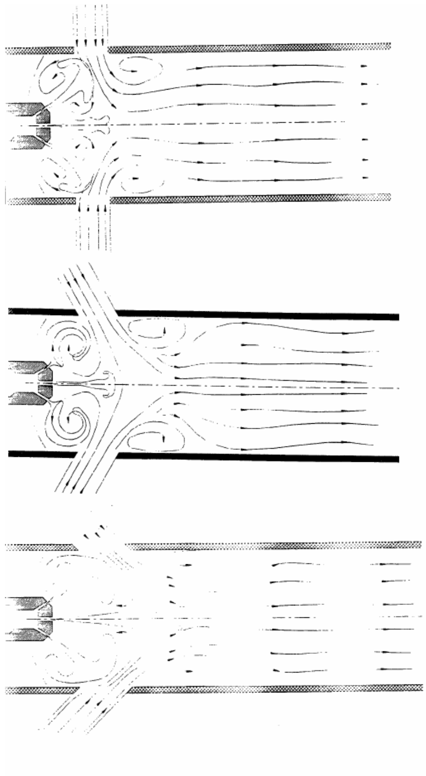

Figure 1-20 Streamlines Inside The Combustor [21]

Wilson studied feed-back control of combustion chambers by fuel modulation in a model combustor [22].

Ristori designed and manufactured a windowed model combustor, where propane (C3H8) is used as fuel, in order to setup an experimental database in non-reacting and reacting flows in 2002. LDV, PLIF, PIV and gas sampling techniques were used [23],[24]. Experimental results were used to validate CFD results and further development of numerical methods.

At ONERA, combustion test rigs with square crossection were used. Two different combustors with same geometry were used for cold flow and reacting flow tests.

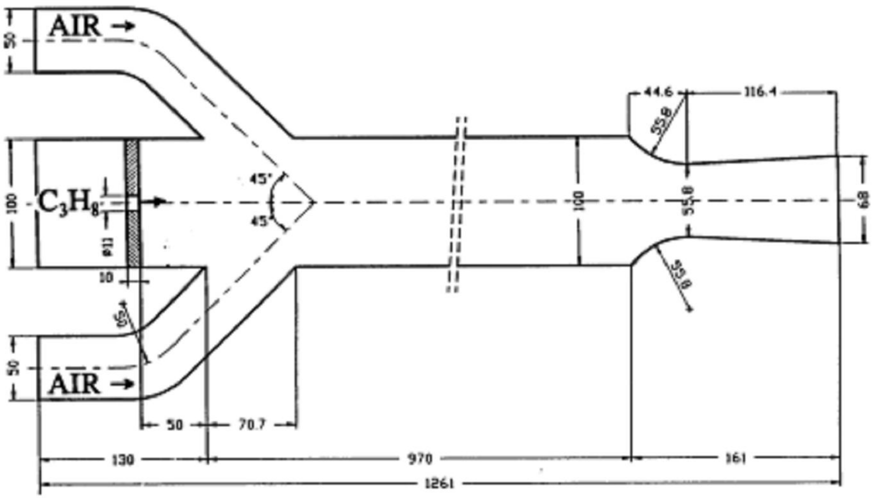

Figure 1-21 Cold Flow Test Combustor Geometry [23]

Cold flow tests were conducted in a plexiglas combustor. LDV, PIV and tracer gas measurements were made. Geometry of the flow field was not variable.

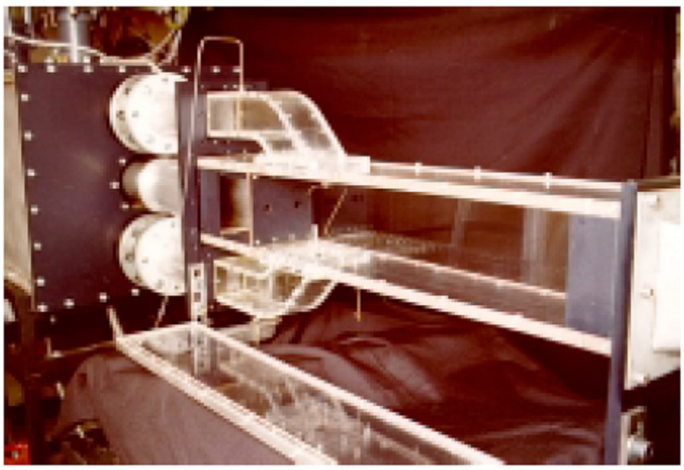

Figure 1-22 Cold Flow Test Combustor [23]

Reacting flow tests were made in a windowed stainless steel combustor to allow combustion visualization.

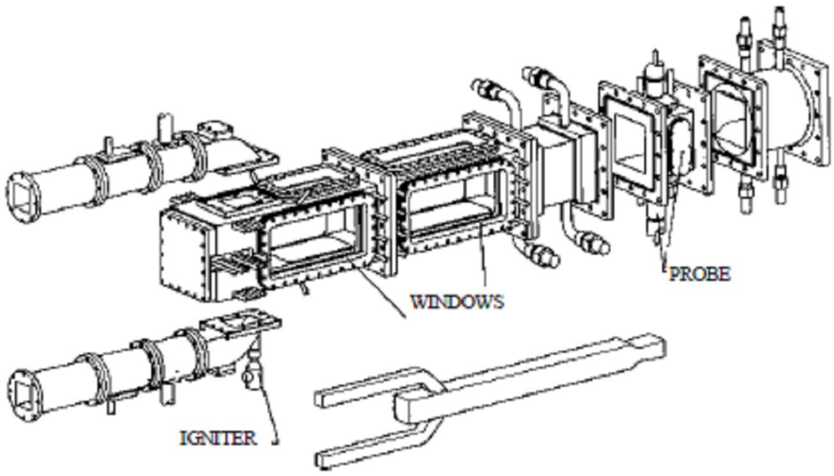

Figure 1-23 Sketch of Reacting Flow Test Combustor [20]

Combustor had square crossection for easy optical access. Ethylene (C_2H_4) was used as fuel. Temperature, pressure and gas composition were measured. Results of the experiments were used in development of numeric models.

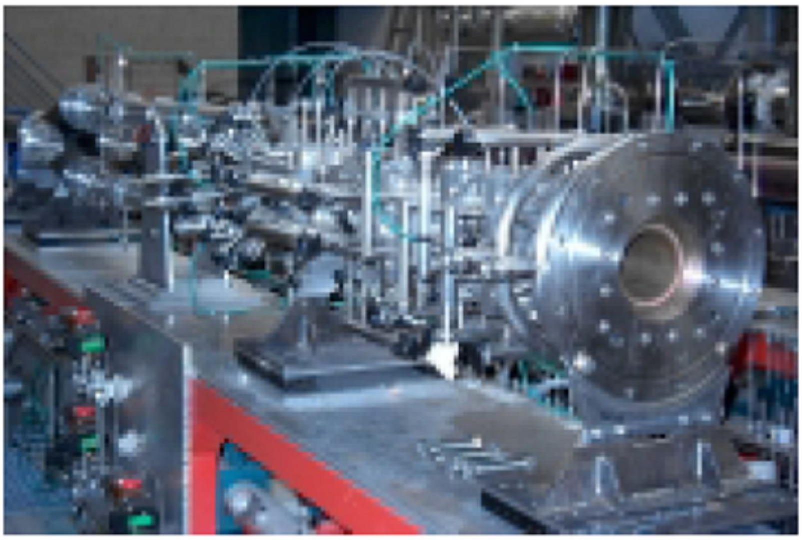

Figure 1-24 Reacting Flow Test Combustor [23]

Combustion tests were made by using C_3H_8 and $C_{10}H_{20}$ fuels. Combustor pressures were 5.7, 3.8 and 1.8 bars. Equivalence ratios 0.5 and 1 are studied for each fuel and pressure case. Efficiencies are not reported in this study. PIV and LDV measurements were used for validation of in-house CFD codes of ONERA [23].

Finally Shoji and Miyayama used a subscale combustor in 2006 to investigate the jet flame characteristics in ducted rockets. Experiments were conducted with different fuel formulations at various combustion chamber pressures and air to fuel ratios. Combustion chamber pressure and air flow rate was measured for efficiency calculation [25],[26].

This combustor was used mainly for propellant development tests. Various propellant formulations with different metal additives has been tested. Air mass flow rate and combustor pressure was measured. Fuel flow rate was calculated from total propellant mass and burn time. As a result of experiments, C* efficiencies of different propellant formulations was determined. [25].

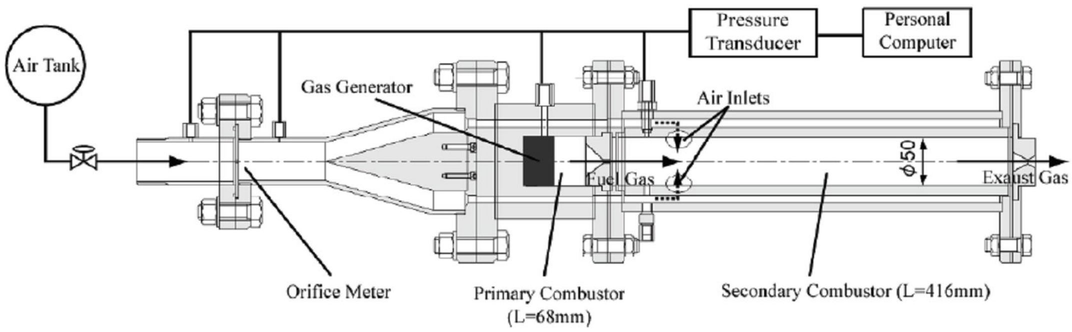

Figure 1-25 Combustor in Nihon University[25]

Combustion in the primary chamber is defined as primary flame whereas combustion in secondary combustor is defined as secondary flame in this study. A secondary flame limit according to combustor and fuel temperatures was reported by Shoji. [26] This limit is given in Figure 1-26. Effect of air to fuel ratio and secondary flame formation on combustion efficiency is given in Figure 1-27. As a conclusion, secondary flame formation has a very important effect on efficiency and should be examined carefully.

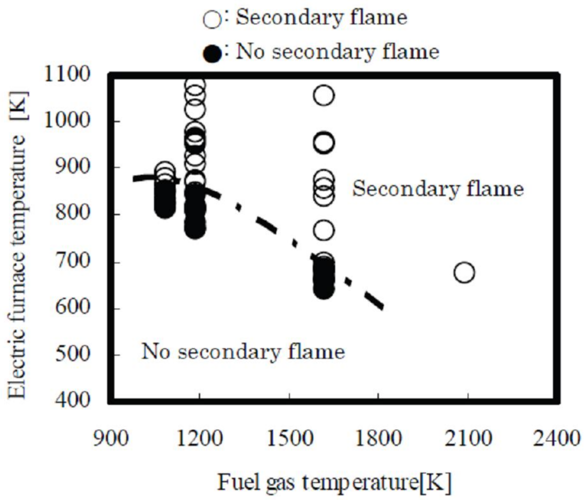

Figure 1-26 Secondary Flame Limit [25]

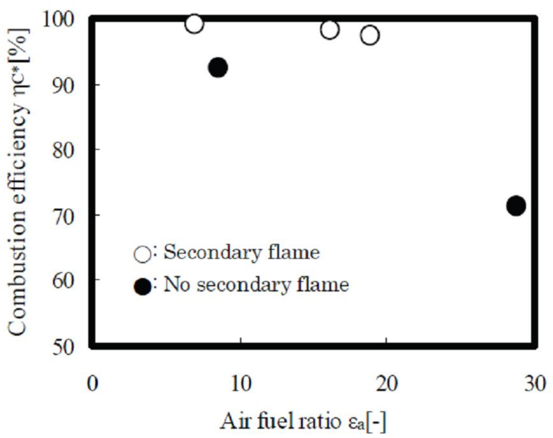

Figure 1-27 Effect Of Secondary Flame Formation on Efficiency [25]

In 1993, Arkun designed and manufactured a subscale engine for experimental studies in laboratory environment. Liquid fuels were used and experimental results were compared to one dimensional numerical simulations [27].

CHAPTER 2

FUNDAMENTALS OF AIR BREATHING ENGINES

2.1 THE ROCKET MOTOR

A rocket motor is a device that produces thrust to accelerate a flight vehicle to a desired velocity. Chemical energy stored in the rocket propellant is turned into thermal energy by combustion. Thermal energy of the high temperature and high pressure gaseous products is turned into kinetic energy in a converging and diverging nozzle. The reaction of exhaust gas momentum and pressure forces on the rocket body produces the thrust [28].

Most of the rocket motors can be classified in three groups which are solid propellant rocket motors, liquid propellant rocket motors and hybrid rocket motors. Solid propellant rocket motors contain both the fuel and the oxidizer mixed in solid phase. This mixture which is called grain is stored in a case.

In liquid propellant rockets oxidizer and fuel is stored in pressurized tanks in liquid phases. The liquid propellants are fed into a chamber where combustion occurs.

Hybrid rockets have its fuel in solid form and its oxidizer in liquid form. Liquid oxidizer is injected over the solid fuel grain [28]. Schematic pictures of each are shown in Figure 2-1, Figure 2-2 and Figure 2-3.

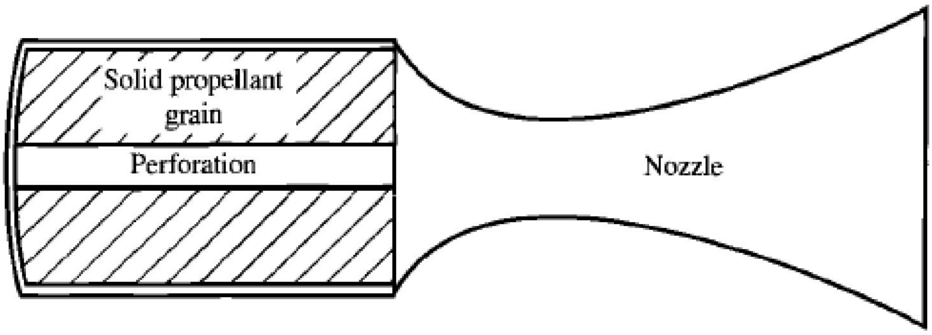

Figure 2-1 Sketch of a Solid Rocket Motor [29]

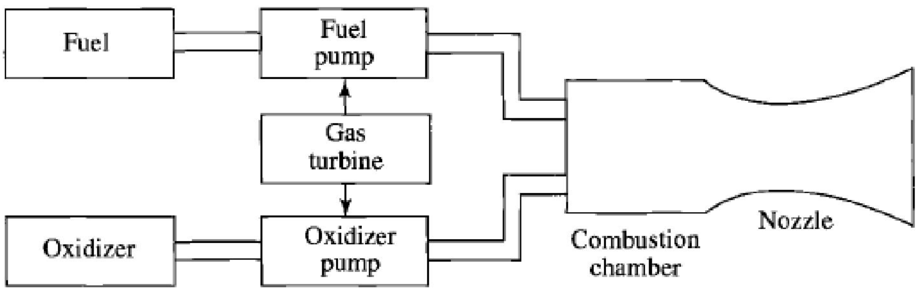

Figure 2-2 Sketch of a Liquid Rocket Motor [29]

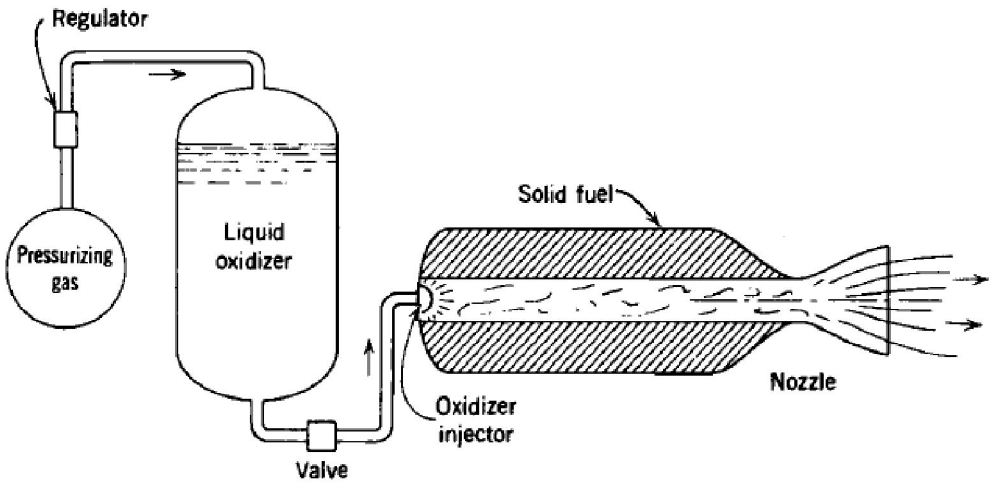

Figure 2-3 Sketch of a Hybrid Rocket Motor [28]

2.1.1 Thrust of the Rocket Motor

Thrust which is produced by a rocket motor is the sum of rate of momentum flow from the nozzle and pressure forces in the nozzle. The control volume and the free body diagram is shown in Figure 2-4.

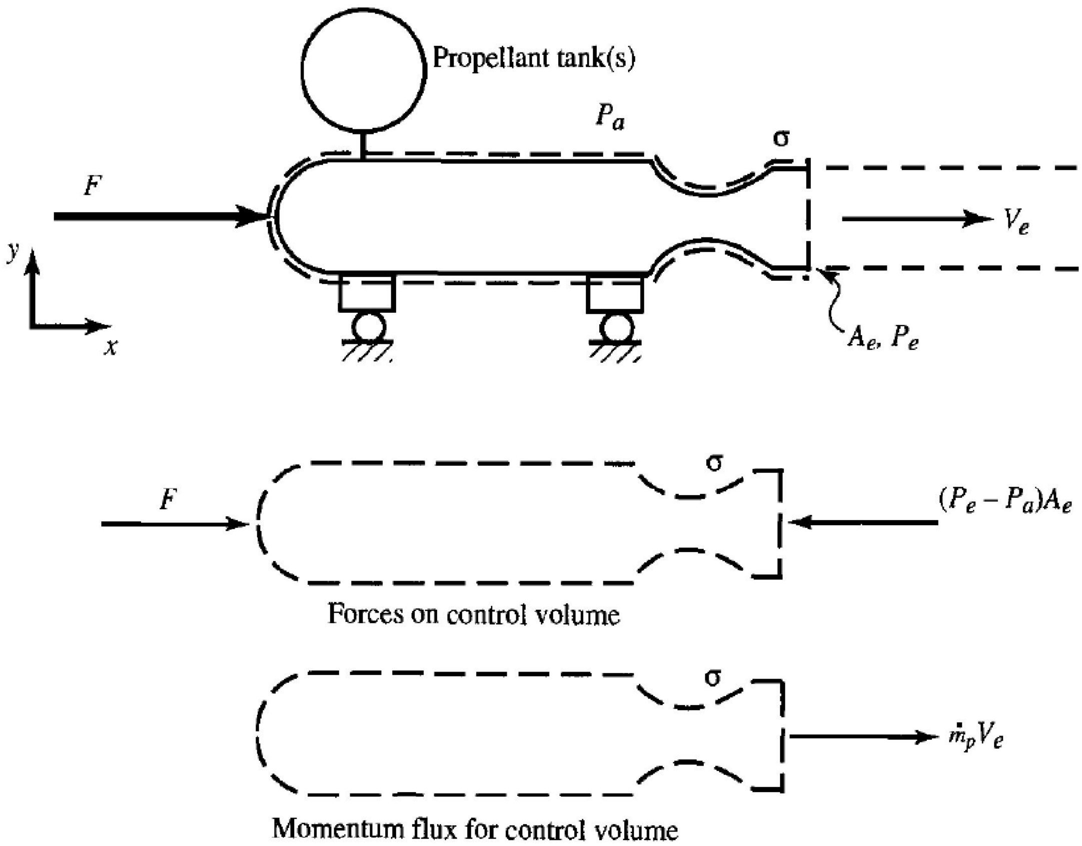

Figure 2-4 Rocket Motor Pressure Forces and Momentum Flux [29]

Thrust of a rocket motor is given by the equation below [29].

$$F = \dot{m} v_e + (P_e - P_{amb}) A_e \tag{2.1}$$

Newton (N) is the unit of the specific impulse in SI system.

2.1.2 Specific Impulse of the Rocket Motor

Specific impulse, I_{sp}, is the amount of thrust force produced by the unit weight of propellant. As specific impulse defines the amount of fuel needed to obtain a thrust for a period of time, it is a commonly used performance parameter [28].

Specific impulse is defined as

$$I_{sp} = \frac{F}{\dot{m} g_0} \tag{2.2}$$

Seconds (s) is the unit of the specific impulse in SI system.

2.1.3 Characteristic Velocity of the Rocket Motor

Characteristic velocity C* is a function of combustion chamber pressure, nozzle throat area and the mass flow rate of the propellant. Theoretical value of C* is dependent to the propellant formulation. The theoretical value can be obtained by thermochemistry calculations. C* is defined by

$$C^* = \frac{P_c A_t}{\dot{m}} \tag{2.3}$$

As C* is a function of easily measured quantities, it is commonly used for both efficiency determination and comparison of the relative performance of different chemical rocket propulsion system designs and propellants [28].

Meters per second (m/s) is the unit of the C* in SI system.

2.2 THE AIR BREATHING ROCKET ENGINE

In 1913, the idea of an air breathing rocket engine originated at the patent of Lorin where a jet engine based on ram compression in supersonic flight was proposed [29]. *"Air-breathing engines, comprises devices which have a duct to confine the flow of air. They use oxygen from the air to burn fuel stored in the flight vehicle."*[28]

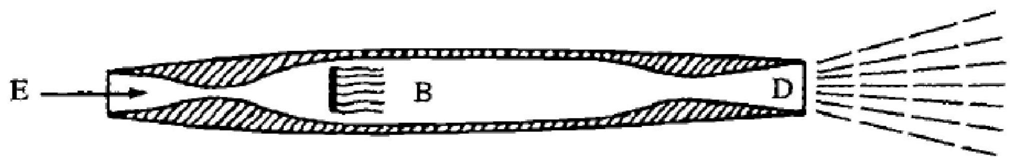

Figure 2-5 Engine of Lorin as Proposed in 1913 Patent

An air breathing rocket engine is conceptually the simplest aircraft engine which operates on a brayton cycle and consists of an inlet or diffuser, a combustor or burner, and a nozzle [29].

Three different configurations with different fuel feeds are present in literature. These configurations use different fuels. They are liquid fueled, solid fueled and ducted rockets.

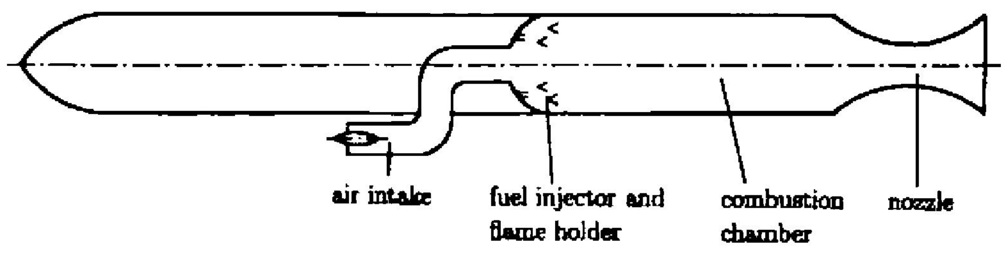

Figure 2-6 Liquid Fueled Air Breathing Rocket Engine [30]

Liquid fuel is injected into the combustion chamber and mixed with the air entering from air intake in liquid fuel air breathing engines . Fuel flow rate is regulated by a valve, hence the thrust is controllable. Hydrocarbon fuels such as kerosene or slurry fuels are used as liquid fuel. Due to the high combustion enthalpy of their fuels, they have very high performance. Most of the operational systems have been using liquid fuels. [30]

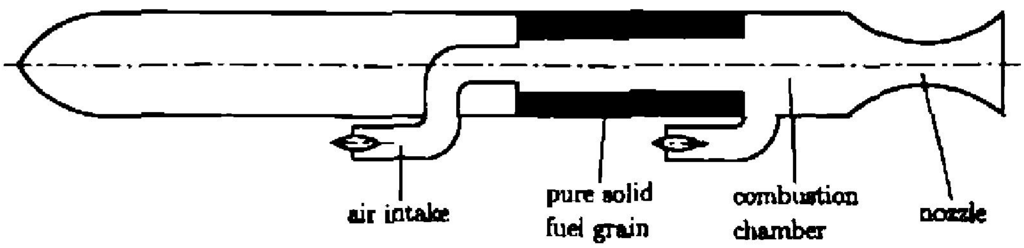

Figure 2-7 Solid Fuel Air Breathing Rocket Engine [30]

Solid fuel air breathing rocket contains a pure solid fuel grain which does not have oxidizing compounds in it. During operation, the solid fuel vaporizes by the heat in the combustion chamber. Vaporized fuel is mixed with air which is flowing through the grain.

Although solid propellant air breathing rockets have advantages over solid propellant rockets in handling and production, they are not used in operational systems as burning rates are not enough to produce thrust levels comparable to other alternatives. [30]

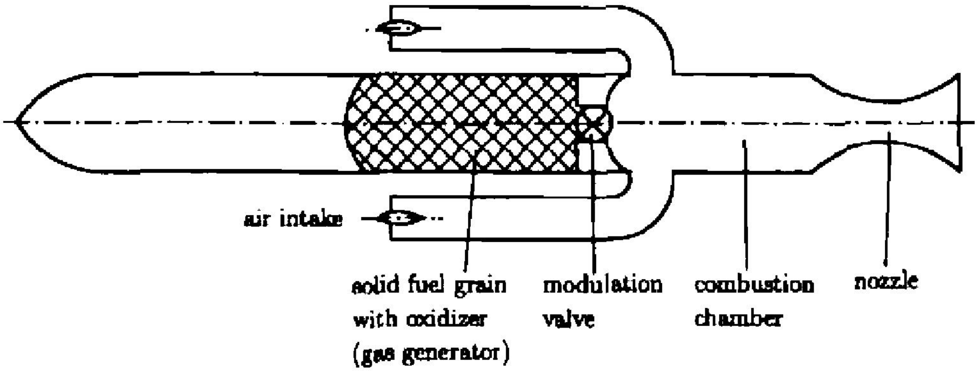

Figure 2-8 Ducted Rocket Engine [30]

The ducted rocket contains a fuel rich solid propellant in a gas generator. In contrast to the solid propellant, smaller amount of oxidizer is needed to react with a portion of the fuel. Heat released from this reaction pyrolyse the remaining fuel. Combustion of the pyrolized fuel is completed in a secondary chamber. As in the case of liquid fuel, thrust of the ducted rocket can also be modulated by using a fuel flow rate controlling valve. [30]

2.2.1 Thrust of the Air Breathing Rocket Engine

Thrust of an air breathing engine is the sum of the net rate of momentum flow through the engine and pressure forces in the nozzle.

Thrust of an air breathing engine is given by the equation below [29].

$$F = \dot{m}_e v_e - \dot{m}_i v_i + (P_e - P_{amb}) A_e \qquad (2.4)$$

Newton (N) is the unit of the specific impulse in SI system.

2.2.2 Specific Impulse of the Air Breathing Rocket Engine

In contrast to the rocket motor, specific impulse of the air breathing engine is defined as

$$I_{sp} = \frac{F}{\dot{m}_f g_0} \tag{2.5}$$

Seconds (s) is the unit of the specific impulse in SI system.

2.2.3 Characteristic Velocity of the Air Breathing Rocket Engine

Similar to the rocket motors, characteristic velocity of the air breathing engine is defined by

$$C^* = \frac{P_c A_{th}}{\dot{m}_t} \tag{2.6}$$

Where

$$\dot{m}_t = \dot{m}_f + \dot{m}_o \tag{2.7}$$

2.2.4 Cycle Analysis of the Air Breathing Rocket Engine

From thermodynamics point of view, air breathing rocket engine is an application of the brayton cycle. In ideal cycle analysis of air breathing rocket engines some assumptions are made.

These assumptions can be given as follows,

- Ideal compressible gas is assumed
- Fuel flow rate can be neglected, hence flow rate is constant
- Constant specific heats are assumed
- Pressure drops are neglected
- Compression and expansion are isentropic
- Nozzle exit pressure is equal to flight atmospheric pressure

Mattingly defines the station numbers in the cycle as in Figure 2-9 [29].

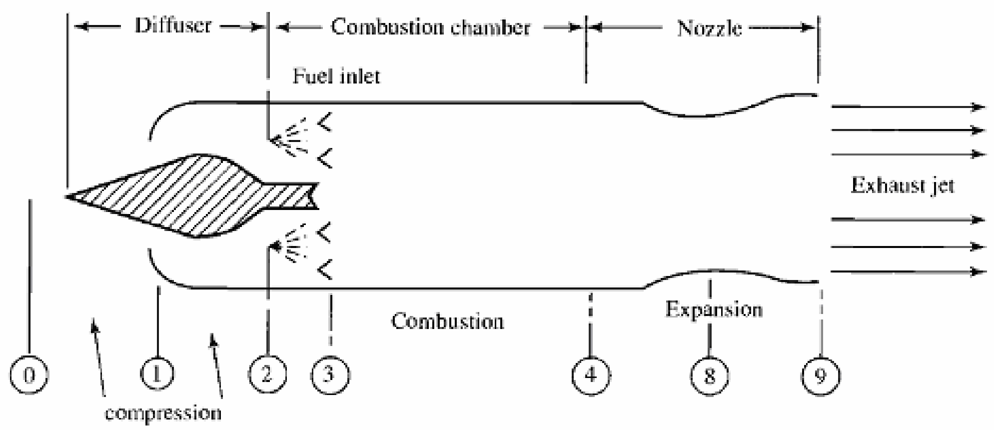

Figure 2-9 Station Numbers of a Air Breathing Rocket Engine [29]

Station 0 is the free stream. In an ideal ramjet, between Station 0 and Station 2 isentropic compression takes place. From Station 2 to Station 4 isobaric combustion occurs. Finally, from Station 4 to Station 9, there is isentropic expansion in the nozzle. On a temperature – entropy diagram these stages can be shown as follows.

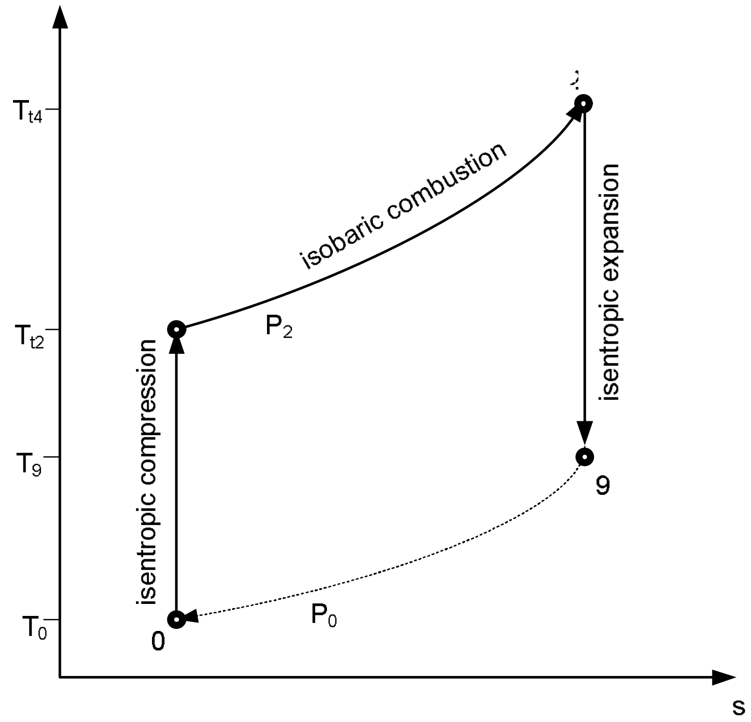

Figure 2-10 Temperature Entropy Diagram of the Ideal Cycle

The area of a closed curve in temperature – entropy diagram gives the net work output. In this case, the net work output is the thrust. To maximize the thrust either P_2 of T_{t4} should be increased. Since P_2 is a result of flight condition, T_{t4} is the technological parameter. Thrust equation of the engine can be rewritten in terms of cycle stations as

$$F = \dot{m}_9 v_9 - \dot{m}_0 v_0 + (P_9 - P_0) A_9 \tag{2.8}$$

In an ideal engine analysis, fuel flow rate can be ignored and constant mass flow rate through the engine can be assumed. Also exit pressure is equal to the freestrem pressure in the ideal engine as the gas expands to same atmospheric conditions with inflowing air.

Hence the thrust equation can be rewritten as

$$F = \dot{m}_0 (v_9 - v_0) = \dot{m}_0 a_0 (\frac{v_9}{a_0} - M_0) = \dot{m}_0 a_0 (\frac{a_9}{a_0} M_9 - M_0) \tag{2.9}$$

In ideal engine cycle analysis, constant gas specific heats are assumed through the engine. Hence ratio of the speed of sounds in Station 9 and Station 0 can be expressed as follows

$$\frac{a_9}{a_0} = \frac{\sqrt{\gamma_9 R_9 T_9}}{\sqrt{\gamma_0 R_0 T_0}} = \sqrt{\frac{T_9}{T_0}} \tag{2.10}$$

From gas dynamics of isentropic flow it is known that

$$\frac{P_t}{P} = \left(\frac{\gamma - 1}{2} M^2 + 1\right)^{\gamma/(\gamma-1)} \tag{2.11}$$

There is no shaft work input or output during the cycle. As the pressure losses are neglected in the ideal cycle analysis, total pressure can be assumed constant through the engine. Meanwhile, static pressure at Station 0 and Station 9 were same. Hence pressure ratios at Station 0 and Station 9 are equal. These equalities can be written as follows.

$$\frac{P_{t0}}{P_0} = \left(\frac{\gamma - 1}{2} M_0^2 + 1\right)^{\gamma/(\gamma-1)} = \frac{P_{t9}}{P_9} = \left(\frac{\gamma - 1}{2} M_9^2 + 1\right)^{\gamma/(\gamma-1)} \tag{2.12}$$

As a result,

$$M_0 = M_9 \tag{2.13}$$

Ratio of the temperatures in Station 9 and Station 0 can be written as

$$\frac{T_9}{T_0} = \frac{T_{t2}}{T_0}\frac{T_{t4}}{T_{t2}}\frac{T_9}{T_{t4}} \tag{2.14}$$

by isentropic compression and expansion assumption

$$\frac{T_9}{T_0} = \left(\frac{P_2}{P_0}\right)^{(\gamma-1)/\gamma} \frac{T_{t4}}{T_{t2}}\left(\frac{P_0}{P_2}\right)^{(\gamma-1)/\gamma} = \frac{T_{t4}}{T_{t2}} \tag{2.15}$$

Implementing these results into the thrust equation gives

$$F = \dot{m}_0 a_0 \left(\frac{a_9}{a_0} M_9 - M_0\right) = \dot{m}_0 a_0 M_0 \left(\sqrt{\frac{T_{t4}}{T_{t2}}} - 1\right) \tag{2.16}$$

To find the relation between total temperature in Station 4 and total temperature in Station 2, energy balance equation between these states which is given below should be used.

$$\dot{m}_0 h_{t2} + \dot{m}_f h_f = \left(\dot{m}_0 + \dot{m}_f\right) h_{t4} \tag{2.17}$$

When the change in total flow rate by fuel addition is neglected and constant specific heat assumption is used, energy balance equation is simplified to the following equation.

$$\dot{m}_0 c_p T_{t2} + \dot{m}_f h_f = \dot{m}_0 c_p T_{t4} \tag{2.18}$$

Fuel to air ratio can be defined as

$$f = \frac{\dot{m}_f}{\dot{m}_0} = \frac{c_p T_{t2}}{h_f}\left(\frac{T_{t4}}{T_{t2}} - 1\right) \tag{2.19}$$

Specific impulse of the air breathing engine can be defined as

$$I_{sp} = \frac{F}{\dot{m}_f g_0} = \frac{F}{\dot{m}_0 f g_0} \tag{2.20}$$

which is given by the equation

$$I_{sp} = \frac{1}{f g_0} a_0 M_0 (\sqrt{\frac{T_{t4}}{T_{t2}}} - 1) = \frac{h_f}{c_p (T_{t4} - T_{t2})} a_0 M_0 (\sqrt{\frac{T_{t4}}{T_{t2}}} - 1) \tag{2.21}$$

Characteristic exhaust velocity of the engine is defined as

$$C^* = \frac{P_c A_{th}}{\dot{m}_t} \tag{2.22}$$

From gas dynamics of isentropic flow, non dimensional mass flow rate is

$$\frac{\dot{m}}{A}\frac{\sqrt{T_t}}{P_t} = \sqrt{\frac{\gamma}{R}} M \left(1 + \frac{\gamma - 1}{2} M^2\right)^{\frac{\gamma+1}{2(\gamma-1)}} \tag{2.23}$$

In a nozzle throat where Mach number is equal to unity, dimensionless mass flow rate is a constant

$$\frac{\dot{m}}{A_{th}}\frac{\sqrt{T_t}}{P_t} = \sqrt{\frac{\gamma}{R}} \left(1 + \frac{\gamma - 1}{2}\right)^{\frac{\gamma+1}{2(\gamma-1)}} \tag{2.24}$$

Hence C* is given by the equation

$$C^* = \frac{P_c A_{th}}{\dot{m}_T} = \sqrt{T_t}\sqrt{\frac{R}{\gamma}}\left(1 + \frac{\gamma - 1}{2}\right)^{\frac{2(\gamma-1)}{\gamma+1}} \tag{2.25}$$

To sum up, three performance parameters which are thrust, specific impulse and characteristic exhaust velocity are given by the following three equation

$$F = \dot{m}_0 a_0 M_0 (\sqrt{\frac{T_{t4}}{T_{t2}}} - 1) \tag{2.26}$$

$$I_{sp} = \frac{1}{f g_0} a_0 M_0 (\sqrt{\frac{T_{t4}}{T_{t2}}} - 1) = \frac{h_f}{c_p (T_{t4} - T_{t2})} a_0 M_0 (\sqrt{\frac{T_{t4}}{T_{t2}}} - 1) \tag{2.27}$$

$$C^* = \sqrt{T_{t4}}\sqrt{\frac{R}{\gamma}}\left(1 + \frac{\gamma - 1}{2}\right)^{\frac{2(\gamma-1)}{\gamma+1}} \tag{2.28}$$

In these equations, M_0, a_0, g_0, T_{t2} are defined by flight conditions. R, γ and c_p are gas properties. $\dot{m}$ and f are design parameters. Finally h_f, T_{t4} are technological parameters. For a higher performance air breathing engine, higher fuel adiabatic combustion enthalpy and higher combustion chamber temperature is needed. This can be achieved by high energy propellant development and high combustion efficiencies.

This is the major reason of the need for sub scale experimental combustors for testing of different propellants and combustion efficiency investigation.

CHAPTER 3

DESIGN OF THE TEST RIG

The test rig is designed to perform combustion experiments with different air to fuel ratios. Conceptual design of the test rig is done for determination of the properties that is needed for conducting the experiments. Detailed design of the test rig was composed from internal ballistic, mechanical and instrumentation system designs which are explained in this chapter.

As a result of examination of the combustion test rigs in the literature, main properties of a combustion test rig for air breathing rocket combustion can be stated as follows:

- Both cold flow and reactive flow tests are conducted on the test rigs.
- Mixing, pressure oscillations, injector design and flow field investigations are done by cold flow tests and reactive flow tests.
- Propellant development, reactive flow simulation validations, combustion efficiency and combustion instability investigations, are done by reactive flow tests.
- Optical access to combustor.
- Both square and circular crossections are present.
- Ability to change geometry, i.e. air inlets and dome heights can be changed.
- Capability to control combustor pressure, fuel and air flow rate.
- Simulated fuel which has similar temperature and similar amount of carbon and hydrogen with the real fuel is commonly used.

- Measurement of pressure, wall pressure distribution, pressure fluctuations, flame temperature, air mass flow rate, velocity and mixture ratio.
- Devices for measurement: pressure transducers, high natural frequency pressure sensors, high temperature thermocouples, venturimeters, pitot tubes, samplings probes, LDV, PIV and PLIF devices have been used for measurements.

These properties were used as reference points for initiation of the combustion test rig design. Combustion test rig is designed to conduct air breathing rocket combustion experiments.

3.1 CONCEPTUAL DESIGN OF THE TEST RIG

The sketch of the combustor is given in Figure 3-1 and Figure 3-2. Windows are present for flow visualization and optical measurements. It has a square crossection for easier optical access.

Either liquid or gaseous fuel can be used in experiments. In case of gaseous fuel feed, a sonic throat is used. Using the sonic throat enables to fix fuel flow rate independently from the combustor pressure. Fuel jet is over expanded after the sonic throat to have subsonic fuel feed to the combustor. Dome plate, where fuel is fed from, is modular and it can be changed to have different dome heights.

Air feed at different pressures can be supplied from a pressure vessel. Two air inlets with opposing position, which is a common configuration, is used. Air inlets are modular and can be changed to have different air inlet angles.

Combustor has a modular sonic throat. Pressure and total mass flow rate can be varied by changing the throat diameter. For a choked throat, pressure and mass flow rate are coupled and both are functions of temperature. As temperature is a result of combustion efficiency mass flow rate can not be precisely set before the experiments.

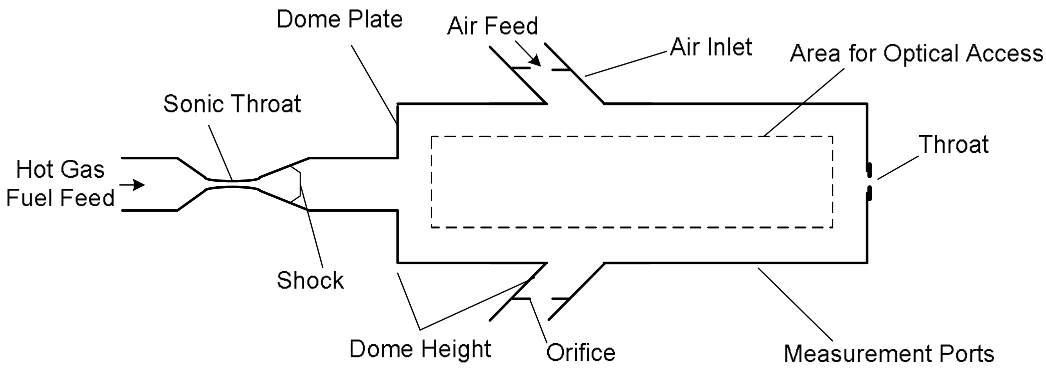

Figure 3-1 Schematic Side View of Combustor

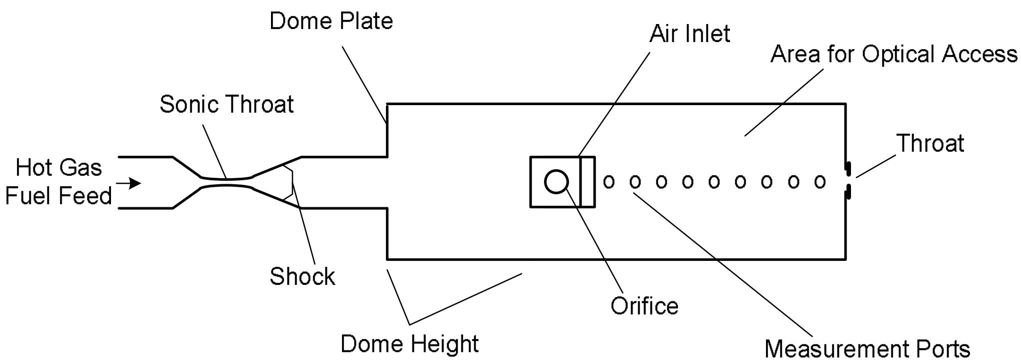

Figure 3-2 Schematic Top View of Combustor

An orifice at the air inlet can be used for choking the flow and adjusting the air flow rate independently from the combustor temperature. However in this case combustor throat may not be choked.

Measurement ports on the combustor let the required measurements to be done in various positions. Temperature, pressure and mass flow rate shall be measured.

Mainly, measurements are done to determine combustion efficiency. The combustion efficiency can be defined in three different manners which are efficiency based on characteristic exhaust velocity, efficiency based on specific impulse and efficiency based on temperature rise [30].

C* efficiency is defined as

$$\eta_{c*} = \frac{c*_{\exp}}{c*_{the}} \tag{3.1}$$

Theoretical characteristic exhaust velocity $C*_{the}$ can be calculated by thermochemisty equilibrium codes such as CEA2 code of NASA [31]. Experimental characteristic exhaust velocity $C*_{exp}$ is defined as

$$c*_{\exp} = \frac{P_{t4} A_8 C_{D8}}{\dot{m}_4} \tag{3.2}$$

where C_D is the nozzle discharge coefficient.

Total pressure at station 4 can be calculated from static pressure at the same station by using following gas dynamics relation

$$P_{t4} = P_4 \left(1 + \frac{\gamma - 1}{2} M_4^2 \right)^{\frac{\gamma}{\gamma - 1}} \tag{3.3}$$

Mach number can be calculated from following equation

$$M_4 = \frac{C_{D8} A_8}{A_4} \left(\frac{2}{\gamma + 1} + \frac{\gamma - 1}{\gamma + 1} M_4^2 \right)^{\frac{\gamma + 1}{2(\gamma - 1)}} \tag{3.4}$$

Specific heat ratio can be calculated by thermochemisty equilibrium codes. Some thermochemisty equilibrium codes can also directly calculate the theoretical value of static pressure over total pressure in finite area combustors.

Hence following equation can be used for total pressure calculation

$$P_{t4,\exp} = P_{4,\exp}\left(\frac{P_t}{P}\right)_{the} \tag{3.5}$$

Efficiency based on specific impulse is defined as

$$\eta_{isp} = \frac{I_{sp_{\exp}}}{I_{sp_{the}}} \tag{3.6}$$

Theoretical value of specific impulse can be calculated by thermochemistry equilibrium codes. Experimental value is calculated by using measured thrust [30].

Efficiency based on temperature rise is defined as below [30].

$$\eta_T = \frac{T_{t4,\exp} - T_{t2}}{T_{t4,the} - T_{t2}} \tag{3.7}$$

$T_{t4,the}$ can be calculated by thermochemistry equilibrium codes[30],[31].

Static pressure and mass flow rate measurements are needed for C* efficiency measurements. Thrust measurement is needed for I_{sp} efficiency calculation. Finally temperature measurement is needed for efficiency based on temperature. The test rig does not have converging diverging nozzle as higher thrust generation is not preferred in a laboratory environment. Hence C* efficiency and efficiency based on temperature rise is used for experiments done by this test rig.

3.2 INTERNAL BALLISTIC DESIGN OF THE TEST RIG

For design considerations, a simulated fuel composition is selected. Both hydrocarbon fuels such as C_3H_8, C_2H_4 and their fuel rich combustion products such as H_2 and CO are used by several authors [8][20][32]. In this study a typical fuel rich hydrocarbon combustion product composition is defined as fuel.

Properties of the air and fuel inlets are given in Table 3-1 where the dimensionless total temperature is defined as

$$\theta = \frac{T - T_{air}}{T_{fuel} - T_{air}} \tag{3.8}$$

Table 3-1 Fuel and Air Properties

CO molar fraction in fuel	35%
H_2 molar fraction in fuel	40%
N_2 molar fraction in fuel	25%
Dimensionless temperature of fuel feed	1
O_2 molar fraction in air	21%
N_2 molar fraction in air	79%
Dimensionless total temperature of air feed	0
Dimensionless stoichiometric combustion temperature	1.93

3.2.1 Combustor geometry

Combustor cross section is defined to have velocities lower than 0.3 Mach throughout the combustor. Combustor has a square cross section. Height and width of the combustor is the reference scale which is taken as 2H. All of the dimensions are defined in terms of half combustor height which is H. Sketch of the combustor geometry is given in Figure 3-3.

Dome height is defined as distance between fuel and air injection points. Dome height and air inlet angle is variable. Dome heights equal to diameter (side length if combustor is square) or half of the diameter (or half of the side length if combustor is square) were common in previous studies. Hence combustor geometry can be adjusted to both. Air inlet angles of 30º, 45º, 60º and 90º have been studied by several authors. Very low efficiencies with 30º air inlets and fluctuating flows at 90º air inlets were reported in the literature.

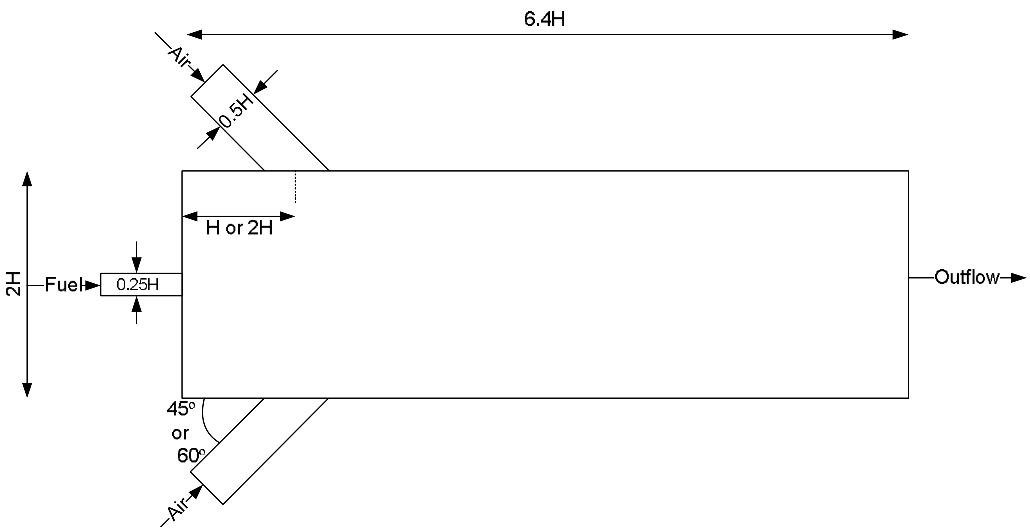

Figure 3-3 Combustor Geometry

Although combustor geometry can be used in every configuration, work in this study is done by 45º and 60º configurations.

3.2.2 Flow field Simulation

Flow field simulations are done to investigate different air inlet angle and dome height configurations with different fuel to air ratio and pressure conditions. Main purpose of the test rig is investigation of different fuels and different air and fuel mixture ratios. Hence flow field simulations were made to ensure that effect of air and fuel mixture ratio on combustion efficiency is greater than geometry and flow field changes. Another purpose of flow field simulations was to determine the probe locations.

3.2.2.1 Determination of Simulation Matrix

Design of Experiments (DOE) approach is used to determine the simulations to be run.

DEO is used to determine the effects of the parameters (factors) on a performance parameter by making experiments by systematically changing the parameters. It is commonly used in:

- Investigation of factor more than one simultaneously.
- Determination of factor interactions
- Determination of design parameters for prototype testing
- Comparison of alternative methods

In single factor experiments, only one parameter is changed at every single experiment. Effect of each parameter is investigated at a single configuration of other parameters. Multi factor experiments allow each parameter to be changed systematically at the same time. An example to one factor experiments is given in Table 3-2. In experiments number 2, 3 and 4 only one parameter is changed.

Table 3-2 One Factor Experiments

Experiment	A: Air Inlet Angle	B: Dome Height	C: F/A ratio
1	45	1H	0.15
2	60	1H	0.15
3	45	2H	0.15
4	45	1H	0.30

When the second experiment is compared with the first experiment, effect of the air inlet angle is determined. Similarly, comparison of third and fourth experiments with the first experiment allows determining the effects of dome height and F/A ratio respectively. However, interactions and cross effects of factors can not be found by these comparisons. An example to multi factor experiments is given in Table 3-3. In this example combined effect of all three parameters can be found.

Table 3-3 Multi Factor Experiments

Experiment	A: Air Inlet Angle	B: Dome Height	C: F/A ratio
1	45	1H	0.15
2	60	2H	0.30

Design of experiments combines single and multi factor experiments. To determine every single and every combined parameter effect, experiments with all combinations of parameters shall be conducted. Such experiment matrices are called full factorial designs. In a full factorial design $\mathbf{a}^{\mathbf{k}}$ experiments should be done where a is the number of factor levels (2,3,..) and k is the number of parameters.

When number of parameters is high and experiments are costly, a fraction of the experiments may be conducted. This is called fractional factorial design. In fractional factorial design, $\mathbf{a}^{\mathbf{k-p}}$ experiments are conducted where p is the fraction. For half factorial design, p is equal to two and for a quarter factorial design, p is equal to four. Half and quarter factorial designs are occasionally used to reduce the number of experiments.

Using DOE also enables reducing the number of numerical simulations and a better interpretation of the parameter effects. Two levels for four parameters in combustion rig design is defined and given in Table 3-4

Table 3-4 Parameter Levels of Design

	Low (-)	High (+)
A: Air Inlet Angle	45°	60°
B: Dome Height	1H	2H
C: Fuel to Air Ratio	0.15	0.30
D: Combustor Pressure	5.6 bar	7 bar

16 runs are needed for a two level four parameter full factorial design. 2^{4-1} half factorial design matrix with 8 runs is given in Table 3-5. In half factorial design, effect of factor D (pressure) is aliased with the triple cross effect of the others.

Table 3-5 Simulation Matrix

	Parameters			
Simulation	A: Angle	B: Dome Height	C: F/A	D (ABC): Pressure
A0101	-	-	-	-
A0201	+	-	-	+
A0301	-	+	-	+
A0401	+	+	-	-
A0102	-	-	+	+
A0202	+	-	+	-
A0302	-	+	+	-
A0402	+	+	+	+

3.2.2.2 Models and Boundary Conditions Used in Simulations

All reactive CFD simulations were made by a commercial solver software [33]. Three dimensional and steady flow is solved by a segregated flow solver. Multi component ideal gas with combustion is solved. Considered species were CO, H_2, N_2, O_2, CO_2 and H_2O. Eddy Break Up (EBU) combustion model was used with standard k-ε turbulence model. Eddy break-up (EBU) combustion model is a turbulent chemical reaction model. In this model, irreversible reactions with turbulent mixing as the rate controlling mechanism are used. The mixing time scale is taken as k/ε. Although these assumptions may lead into crude results for big hydrocarbon molecules, EBU model can be used sufficiently for smaller molecules like methane.

Equations which are solved by the CFD code are presented as follows.

Continuity equation,

$$\frac{\partial \rho}{\partial t} + \frac{\partial}{\partial x_j}(\rho u_j) = s_m \tag{3.9}$$

Navier-Stokes equation,

$$\frac{\partial \rho u_i}{\partial t} + \frac{\partial}{\partial x_j}(\rho u_j u_i - \tau_{ij}) = -\frac{\partial p}{\partial x_i} + s_m \tag{3.10}$$

and the energy equation

$$\frac{\partial \rho h}{\partial t} + \frac{\partial}{\partial x_j}(\rho u_j h - F_{h,j}) = \frac{\partial p}{\partial t} + u_j \frac{\partial p}{\partial x_i} + \tau_{ij}\frac{\partial u_i}{\partial x_j} s_h \tag{3.11}$$

are solved by the segregated flow solver [33].

Stress tensor component in the Navier-Stokes equation is defined as

$$\tau_{ij} = 2\mu s_{ij} - \frac{2}{3}\mu \frac{\partial u_k}{\partial x_k}\delta_{ij} - \bar{\rho}\overline{u_i' u_j'} \tag{3.12}$$

and enthalpy in the energy equation is defined as

$$h \equiv \overline{c_p} T - c_p^0 T_0 + \sum Y_m H_m = h_{th} + \sum Y_m H_m \tag{3.13}$$

Multi component ideal gas model solves the mass transfer equation

$$\frac{\partial}{\partial t}(\rho Y_m) + \frac{\partial}{\partial x_j}(\rho u_j Y_m + F_{m,j}) = s_m \tag{3.14}$$

where diffusional flux component is defined as

$$F_{m,j} = \rho Y_m V_{m,j} + 2\bar{\rho}\overline{u_j' Y_m'} \tag{3.15}$$

Turbulent terms are computed by using a k-ε turbulence model. In this model

$$-\bar{\rho}\overline{u_i' u_j'} = \mu_t S_{ij} - \frac{2}{3}(\mu_t \frac{\partial u_k}{\partial x_k} + \rho k)\delta_{ij} \tag{3.16}$$

and

$$\bar{\rho}\overline{u_j' Y_m'} = -\frac{\mu_t}{\sigma_{m,t}} \frac{\partial Y_m}{\partial x_j} \tag{3.17}$$

where turbulent kinetic energy k is

$$k = \frac{\overline{u_i' u_i'}}{2} \tag{3.18}$$

mean strain is

$$S_{ij} = \frac{\partial u_i}{\partial x_j} + \frac{\partial u_j}{\partial x_i} \tag{3.19}$$

and turbulent viscosity is

$$\mu_t = f_\mu \frac{C_\mu \rho k^2}{\varepsilon} \tag{3.20}$$

In the equation which turbulent viscosity is defined, C_μ is an empirical constant and f_μ is the damping function [33].

Eddy break-up combustion model solves the fuel consumption rate equation

$$R_F = -\frac{\rho\varepsilon}{k} A_{ebu} \min\left[Y_F, \frac{Y_O}{s_O}, B_{ebu} \frac{Y_P}{s_p} \right] \tag{3.21}$$

where A_{ebu} and B_{ebu} are empirical constants 4 and 0.5.

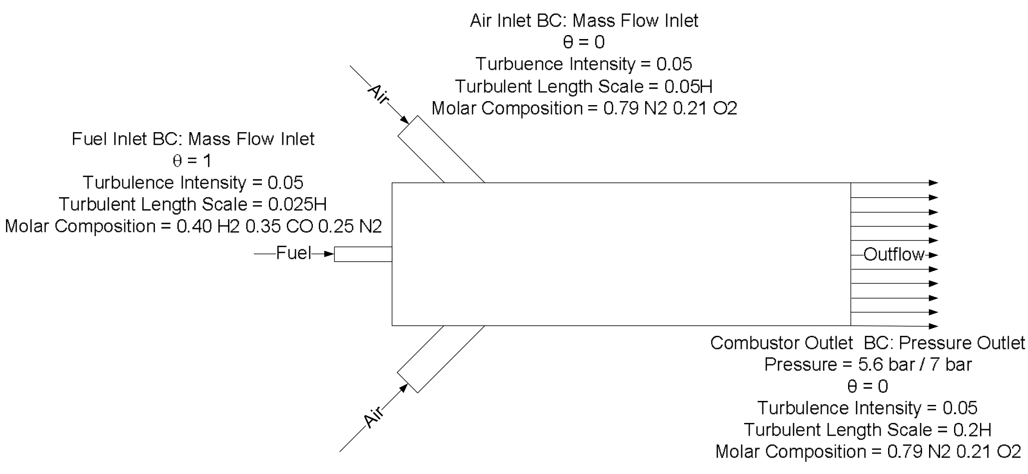

Figure 3-4 Boundary Conditions

In the definition of the problem mass flow inlet boundary condition is used for air and fuel inlets. Pressure outlet boundary condition is used for combustor exit. These boundary conditions are given in Figure 3-4. Turbulence intensity was assumed as 0.05 and turbulent length scales were estimated as 0.1 of corresponding hydraulic diameter for the boundary conditions.

3.2.2.3 Simulations Results

Combustion efficiency results, Mach number and temperature distributions, streamlines in combustor and DOE factor effect graphs are given below. Combustion efficiencies at different axial positions are given in Table 3-6. These values are used for DOE calculations. Obviously, efficiencies increase by combustion length.

Table 3-6 Combustion Efficiencies

Efficiency	η_T			η_{C^*}		
Location (x/H)	3	4	5	3	4	5
A0101	0.73	0.84	0.91	0.88	0.93	0.96
A0201	0.76	0.87	0.91	0.89	0.94	0.96
A0301	0.67	0.83	0.90	0.84	0.92	0.96
A0401	0.75	0.87	0.90	0.88	0.94	0.96
A0102	0.87	0.94	0.99	0.94	0.97	0.99
A0202	0.84	0.93	0.98	0.93	0.97	0.99
A0302	0.84	0.93	0.99	0.93	0.97	0.99
A0402	0.83	0.91	0.98	0.92	0.96	0.99

Mach number distributions in all cases are given in Figure 3-5. It is seen that velocities are higher around the fuel jet. However velocity in the combustor does not exceed 0.3 Mach. Velocities near the walls are low enough for stagnation temperature and pressure measurement with the probes located on the side walls.

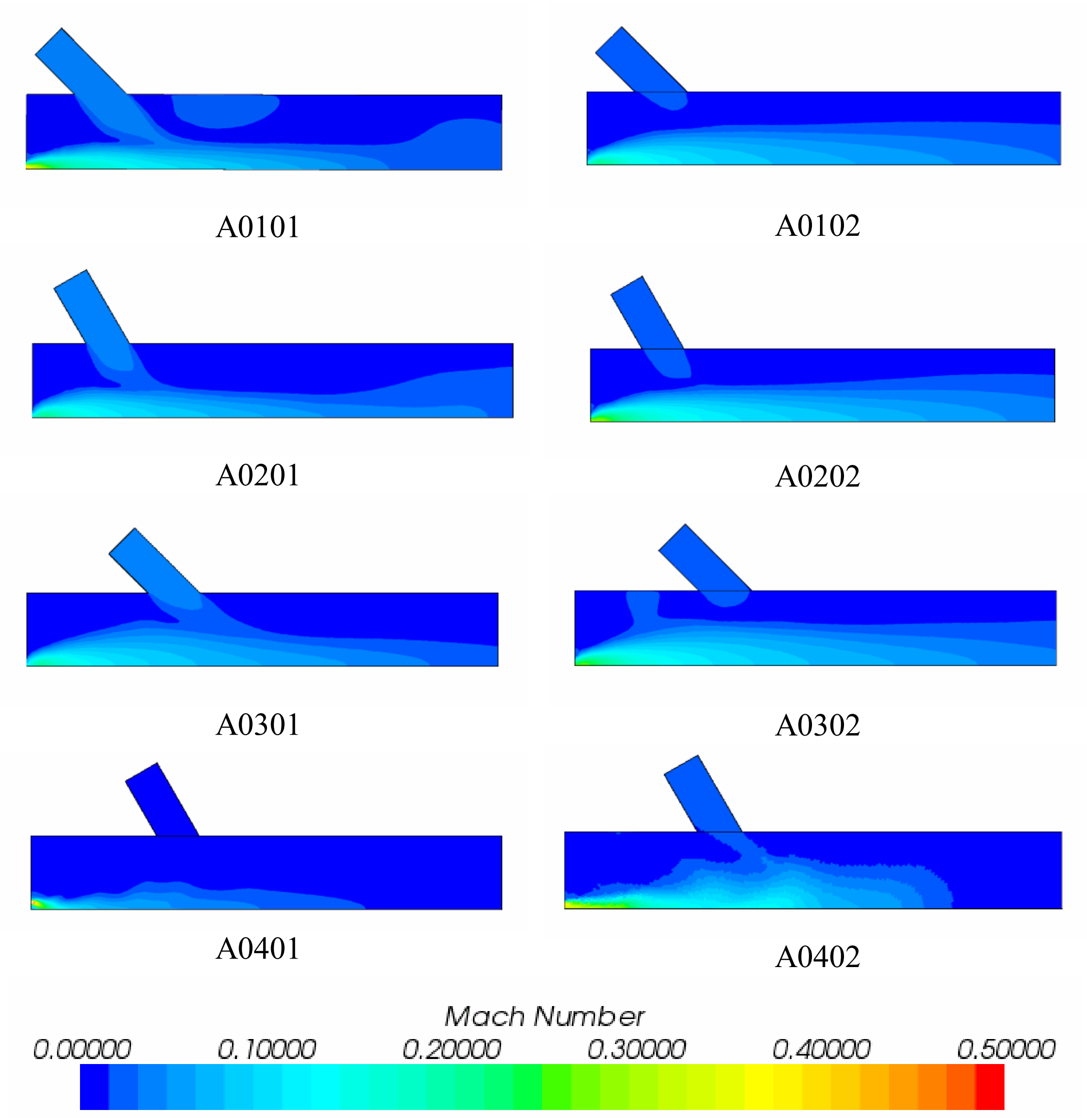

Figure 3-5 Mach Number Distribution in Combustor

Dimensionless temperature distributions are given in Figure 3-6. Higher fuel to air ratio cases have higher temperatures at the exit. They also have higher temperatures in the dome region. 60° air inlet angle and 2H dome height combination has the highest dome temperatures and most uniform outlet temperature. Although temperature is slightly higher in the core region, temperature over the walls at combustor exit is close to the mean exit temperature.

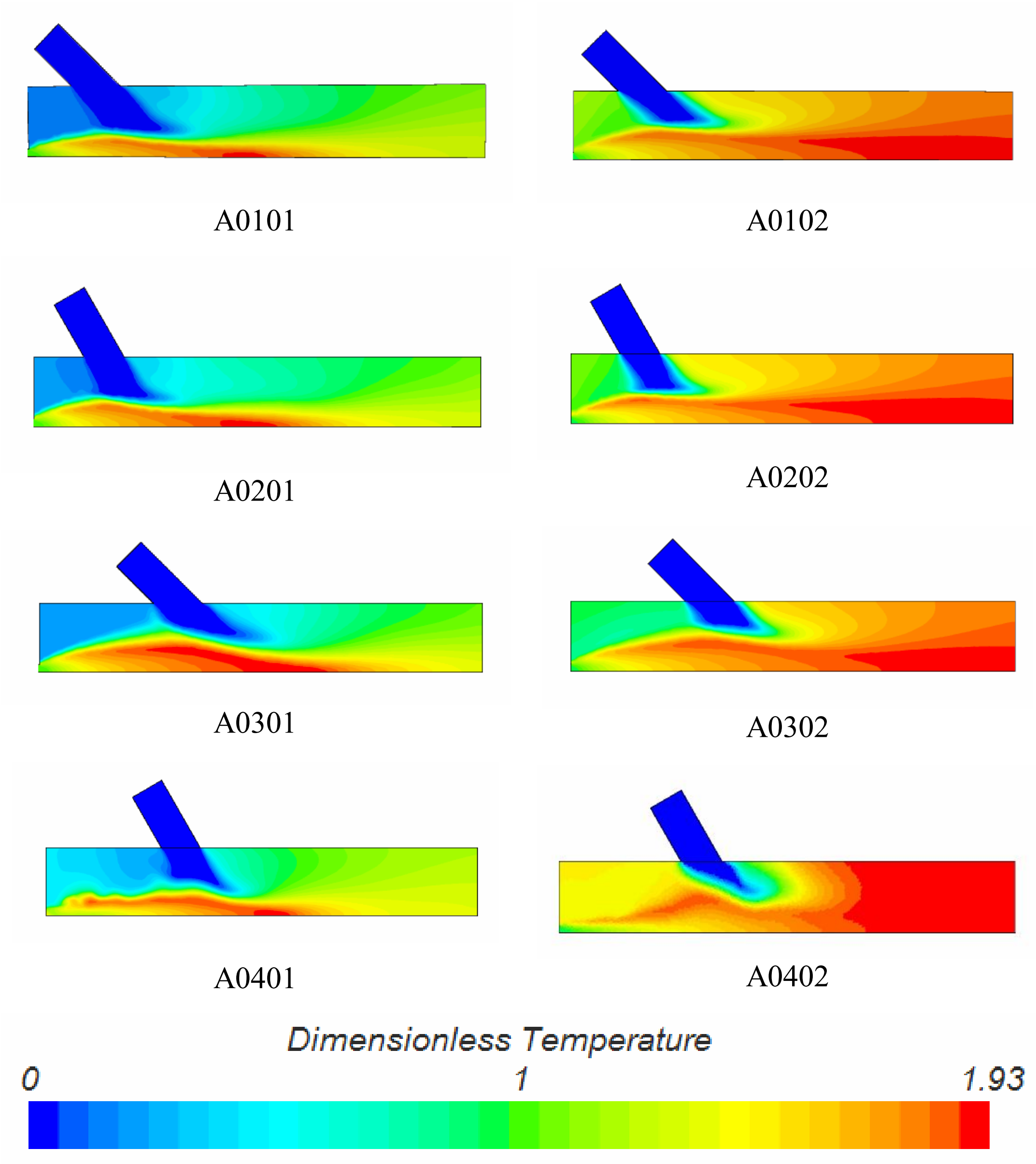

Figure 3-6 Dimensionless Total Temperature Distribution in Combustor

Streamlines in the combustor are given in Figure 3-7. In every case, there exists an air recirculation in the dome region. These air circulations are needed to achieve mixing between the fuel and air. It is also seen that hot fuel jet is wider where dome height is higher.

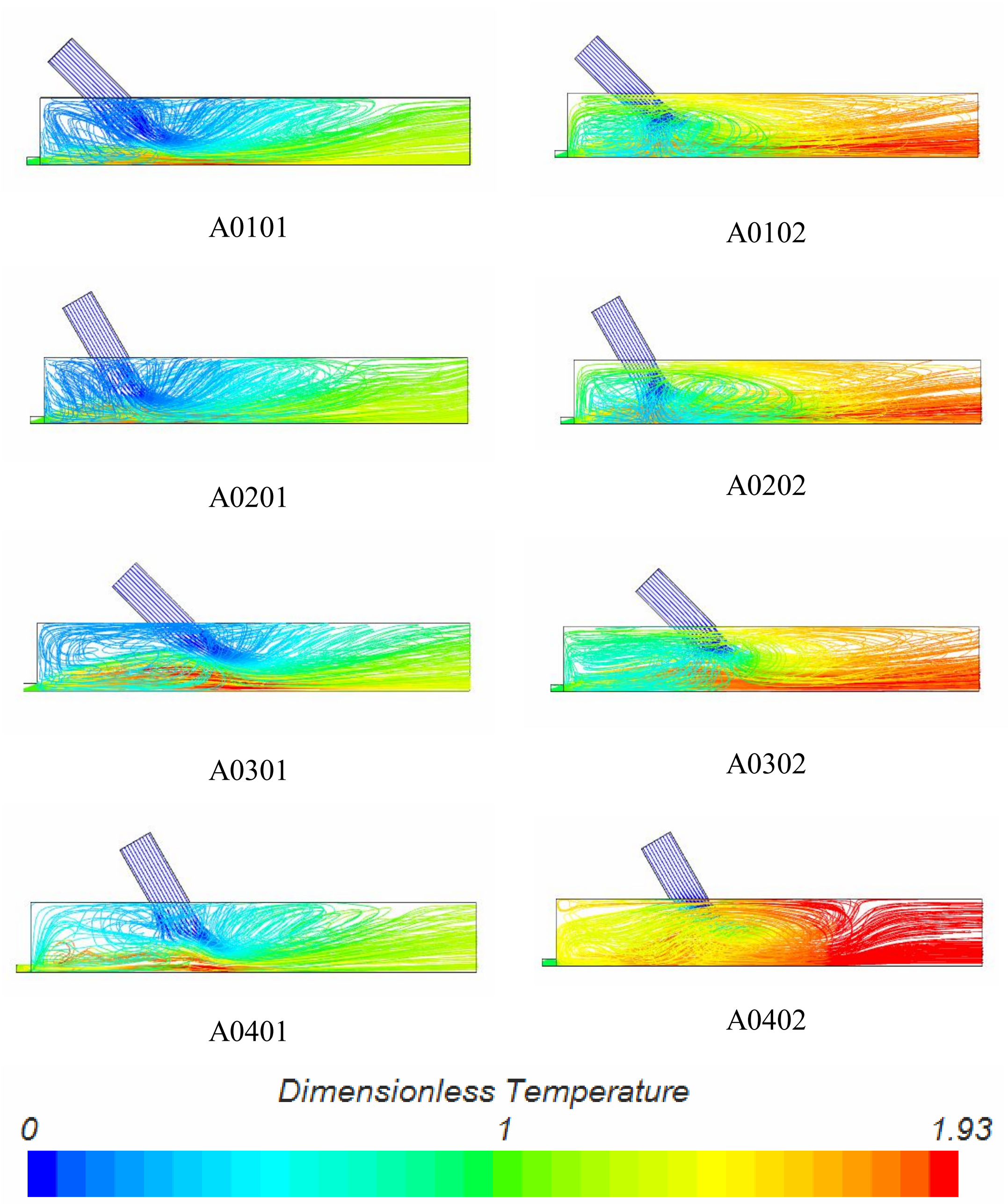

Figure 3-7 Streamlines in Combustor

Results of simulations can be statistically analyzed as the simulation matrix was constructed by using DOE. An ANOVA (ANalysis Of VAriance) table is constructed and given in Table 3-7. By the ANOVA table, distributions can be compared. DOF is the degree of freedom of a source i.e. the number parameters causing any variation. F value is the ratio of the expected variance to unexpected variance. In an ANOVA analysis, F value of factor effects are compared to a reference value that is obtained from Snedecor's F distribution tables. This reference value is a function of degree of freedom of the parameter, error term and the confidence level [34]. F value of each source is compared to the reference value as a hypothesis test. Comparison for the model points out if the model is significant which means the data has a variation other than error.

Table 3-7 ANOVA Table of Thermal Efficiency

Response: Thermal Efficiency, Half factorial design resolution III					
Source	Sum of Squares	DOF	Mean Square	F Value	significance
Model	0.014	5	2.74E-003	176.99	significant
A: Angle	5.551E-005	1	5.551E-005	3.59	
B: Dome Height	1.873E-004	1	1.873E-004	12.10	
C: F/A	0.012	1	0.012	782.35	
D: Pressure	6.026E-005	1	6.026E-005	3.89	
AC: Interaction	1.284E-005	1	1.28E-003	82.99	
Error	3.049E-005	2	1.547E-005		
Cor. Total	0.014	7			

It is seen that most effective factor on efficiency is fuel to air ratio which has the highest F value. Factor effect graphs of fuel to air ratio, air inlet angle and cross effect of dome height with fuel to air ratio are given in Figure 3-8, Figure 3-9 and Figure 3-10 respectively.

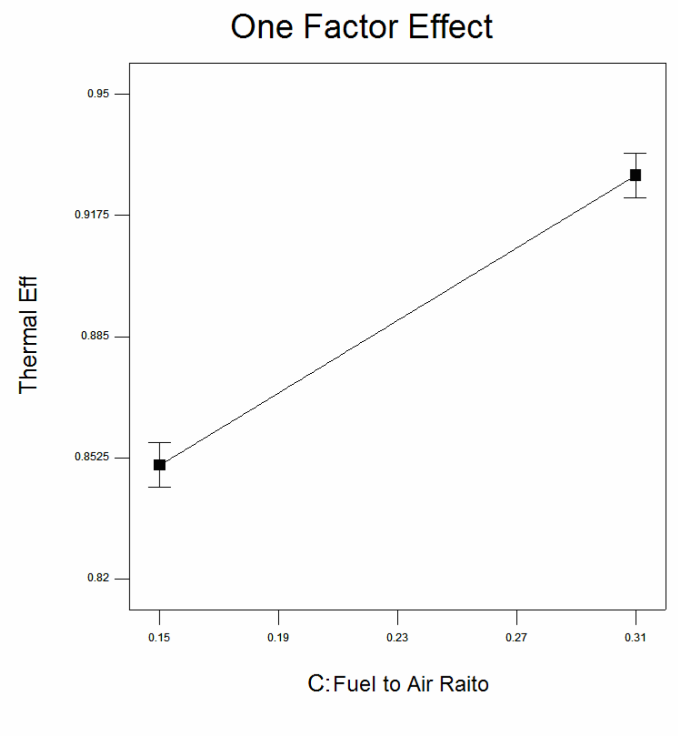

Figure 3-8 Effect of Factor C: Fuel to Air Ratio

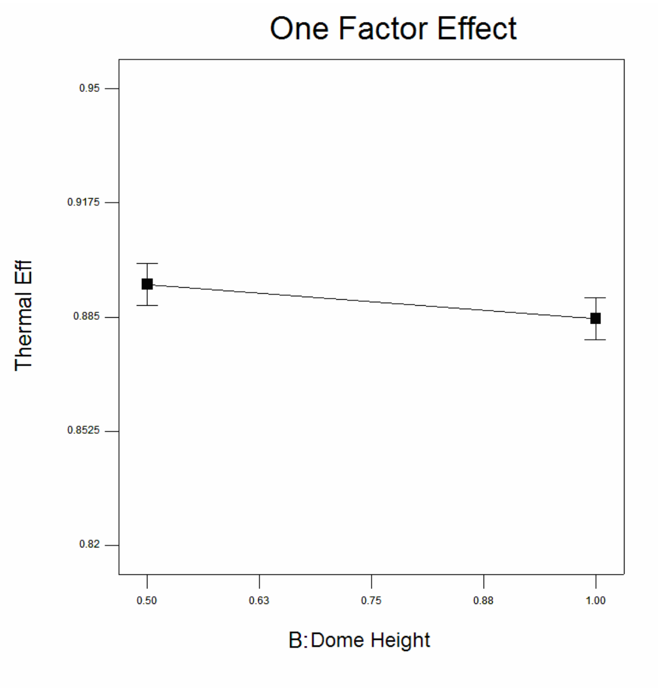

Figure 3-9 Effect of Factor B: Dome Height

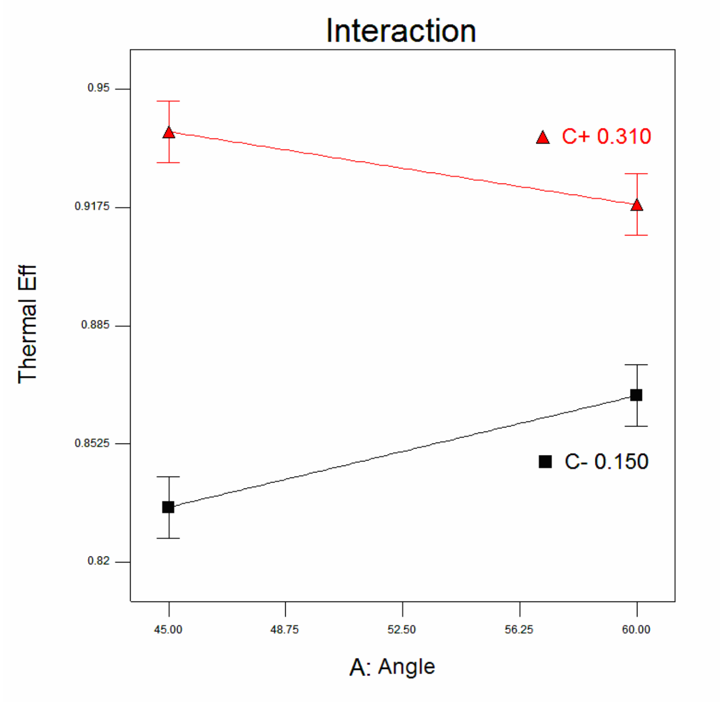

Figure 3-10 Cross Effect of Factor A: Dome Height and C: Fuel to Air Ratio

It is seen from factor effect graphs that higher fuel to air ratio results in a higher efficiency. Increasing dome height has a minor decreasing effect on efficiency. Effects of other parameters are not significant. Air inlet angle has a cross effect with fuel to air ratio. It has different trends with different fuel to air ratios.

60º air inlet angle and 2H dome height is used for the experiments as it was the combination with hottest dome region and most uniform exit conditions.

3.3 MECHANICAL DESIGN OF THE TEST RIG

Solid model of the combustor is given in Figure 3-11. Stainless steel 310S is used in all metallic parts except air inlets to prevent corrosion from high temperature oxygen rich gas flow inside the combustor.

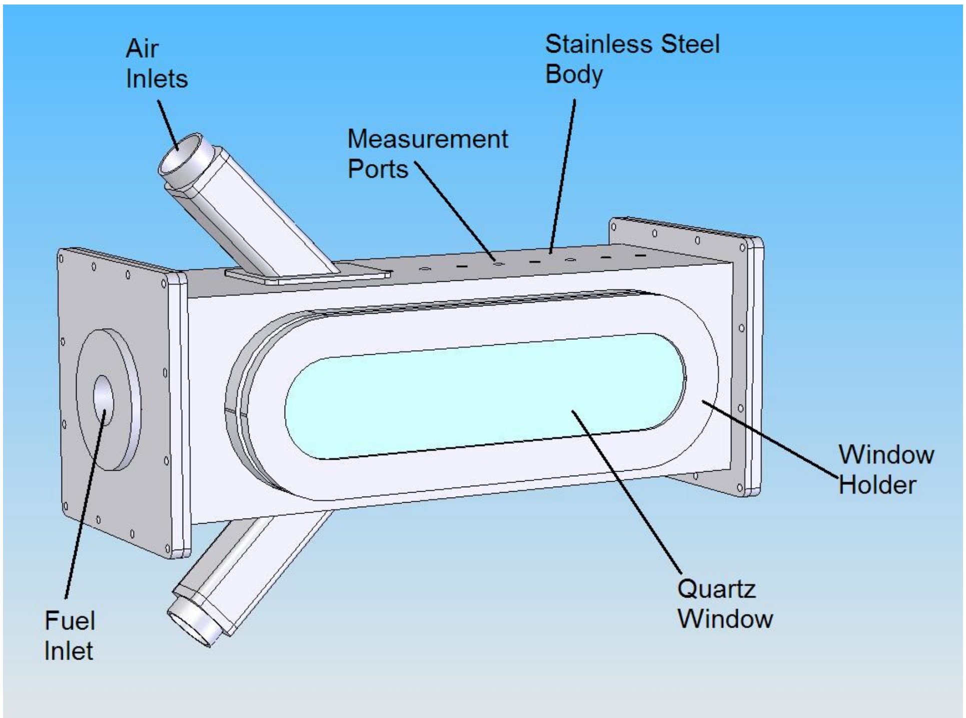

Figure 3-11 Solid Model of Combustor

Grade 12-8 bolts are used to reduce bolt numbers. 16 M4 bolts for air inlets and 10 M8 bolts for fuel inlet and nozzle flanges are selected. Tightening torque was calculated as 42 Nm for 10 bar maximum combustor pressure.

Quartz is selected as window material because of its superior thermal shock resistance and higher melting point than ordinary glass and borosilicate.

Special square and rectangular o-rings made from 70 shA silicon are designed and manufactured for fuel inlet plate, nozzle plate and air inlets.

Picture of the combustor is given in Figure 3-12. Eight measurement ports are present in each side of the combustor.

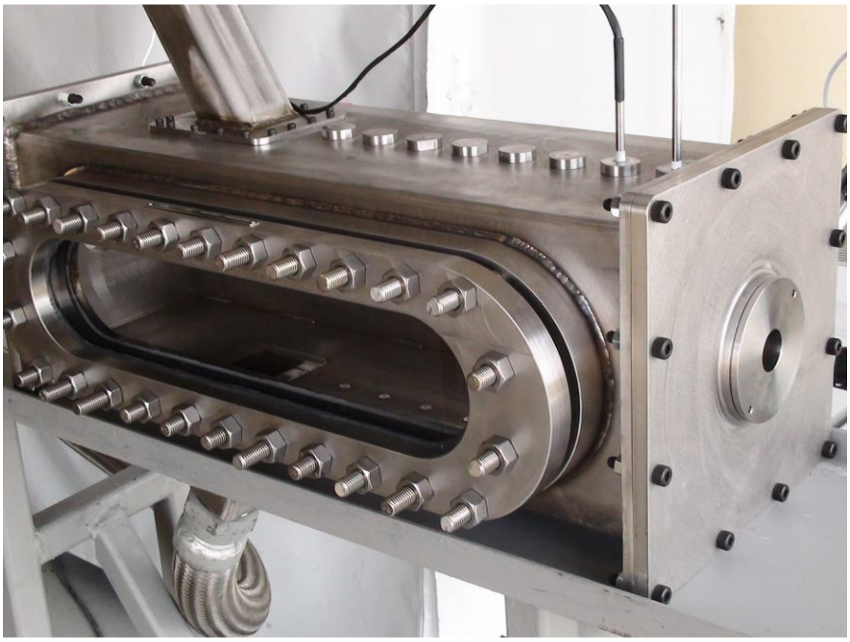

Figure 3-12 Combustor

A pressure sensor (on the right side) and a temperature sensor (on the left side) mounted on the measurement ports is shown in Figure 3-13

Figure 3-13 Pressure and Temperature Sensor on Combustor

3.4 INSTRUMENTATION SYSTEM DESIGN OF THE TEST RIG

Temperature and pressure measurements are conducted from the combustor. Signals are conditioned and data is collected by a data acquisition card.

3.4.1 Temperature Measurements

Most common temperature measurement transducers in engineering applications are thermocouples. They are easy to use and have various types for different needs. There are various types of thermocouples standardized by ASME (see Table 3-8).

A thermocouple is made from two dissimilar metal wires joined in measurement point. The dissimilar metals produce a voltage in presence of a temperature difference (the Seebeck effect). The voltage is a function of both temperatures at the measurement end and terminal end. Hence temperature at terminal point of the thermocouple shall be known. This is called cold junction compensation. It can be done by placing the cold junction in an ice bath or by measuring the temperature by another device.

Table 3-8 ASME Thermocouple Types

Type	Conductors – Positive	Conductors – Negative
B	Platinum-30% Rhodium	Platinum-6% Rhodium
E	Nickel-Chromium alloy	Copper-Nickel alloy
J	Iron	Copper-Nickel alloy
K	Nickel-Chromium alloy	Nickel-Aluminum alloy
N	Nickel-Chromium-Silicon alloy	Nickel-Silicon-Magnesium alloy
R	Platinum-13% Rhodium	Platinum
S	Platinum-10% Rhodium	Platinum

Among these types, B, R and S type thermocouples can be used at elevated temperatures. R type thermocouples are used in this study. Temperatures up to 2000 K can be measured. For higher temperature measurements specially made

Tungsten Rhenium thermocouples with measurement capacity up to 2800 K are used. Another important specification of thermocouples is their crossection diameter. Smaller diameter thermocouples have quicker responses but they are broken more frequently. As the velocities in the combustor are low and test times are short, 0.2 and 0.1 mm diameter thermocouples with very quick response is used. The thermocouple wires are shown in Figure 3-14.

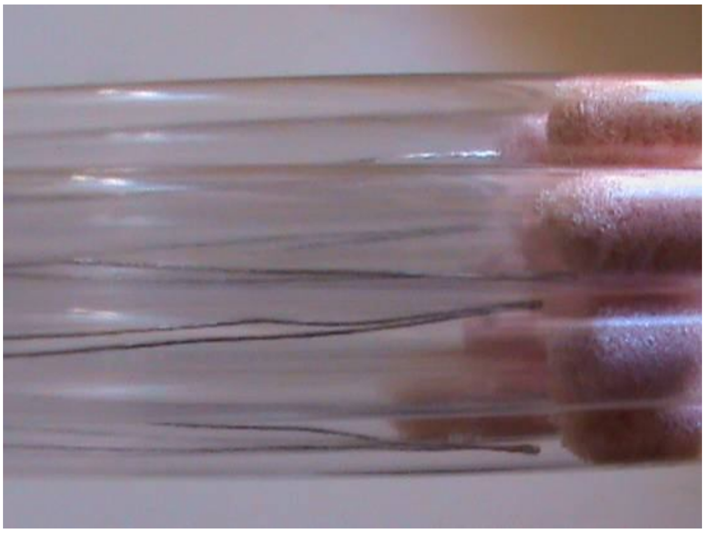

Figure 3-14 Low Response Time Type R Thermocouples

The probe designed for temperature measurements near the combustor surface is shown in Figure 3-15 and the submerged probe for temperature measurements from flame core is shown in Figure 3-16.

Thermocouples are calibrated to measure temperature while their junction at cold end is at 0 C^o. This may be done by placing the thermocouple terminal points into an ice bath. However modern data acquisition equipment allows the cold junction temperature to be measured and used for compensation of actual thermocouple voltage. This is called cold junction compensation.

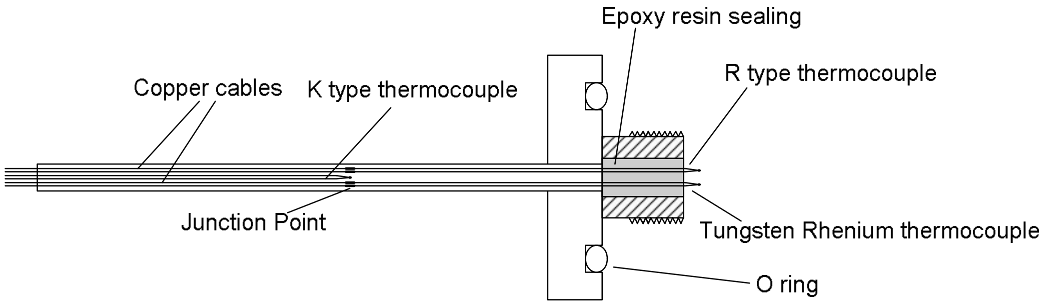

Figure 3-15 Near Surface Temperature Probe

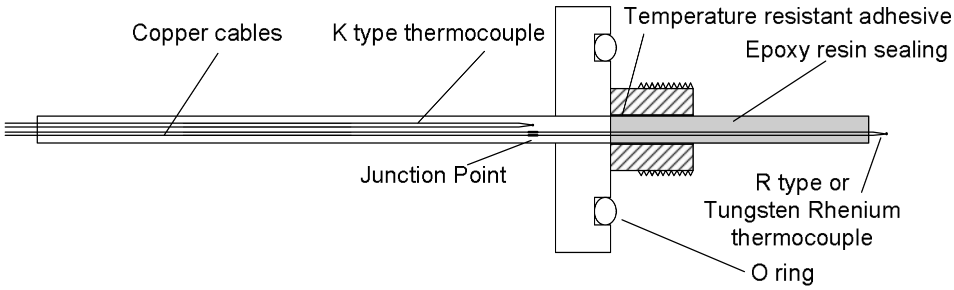

Figure 3-16 Submerged Temperature Probe

Both probes have a K type thermocouple for cold junction compensation of R type and Tungsten Rhenium thermocouples. Cold junction compensation of the K type thermocouple is done by a resistant type sensor built in the signal conditioning hardware.

A picture of the temperature probe is given in Figure 3-17. A protective cap is used while the probe is not connected to combustor. In early probes, thermocouple wires with 0.2 mm crossection were used. In this final configuration 0.1 mm wires are used.

Figure 3-17 Temperature Probe: Parts (top), Assembly (mid), With Cap (bottom)

Temperature measurement by infrared (IR) thermometry is used to compare the dynamic response of the thermocouples. IR thermography is the most developed non-intrusive temperature measurement technique. Although this technique is frequently used for surface temperature measurements, gas temperature can also be measured if the gas is hot and radiating infrared light.

A hot body emits electromagnetic radiation at different wave lengths. Spectral distribution emissive power of a black body is given by the Planck's law

$$M(\lambda,T)=\frac{C_1}{\lambda^5(e^{C_2/\lambda T}-1)} \tag{3.22}$$

Integration of the emissive power over the whole spectrum, which is Stefan-Boltzman law

$$M^0 = \int_0^\infty M_\lambda^0 d\lambda = \sigma T^4 \tag{3.23}$$

gives the total radiation.

IR cameras measure the intensity of the light at band of wavelength. Hence emissive power at a band is measured. This allows calculating total emissive power of a black body by using Planck law. Temperature of a blackbody is then found by Wien law. In solids surface measurements, these relations can be used directly by making gray body assumption. According to this assumption, total emission from a grey body is a ratio of the total emission from a black body at the same temperature. This ratio is constant between zero and one. It is defined as emissivity.

However hot gases are far from grey body assumption when the composition contains molecules composed of different atoms. As well as the exited electrons traveling between the atomic shells, vibration and rotation of these molecules contributes to electromagnetic emission and absorption. Hence emissive power of the gas can not be modeled by Planck law.

As a result, temperature measurements from hot gases should be validated by thermocouple measurements. Otherwise it can only be used for qualitative measurements and flow visualization.

A long wave infrared (LWIR) 8-12 micrometer wavelength camera with a microbolometer sensor is used in this study. Microbolometers are uncooled sensors which measures total energy delivered by infrared light photons. A picture of the camera that is used in this study is given in Figure 3-18.

Figure 3-18 FLIR A 380 LWIR Camera

3.4.2 Pressure Measurements

Pressure measurements from the combustor is essentially needed for C* calculations. In many cases, pressure in the combustor fluctuates due to unsteady flow of colliding jets, ignition problems and combustion instabilities. Fluctuations from combustion instabilities usually have higher frequencies. Two dominant frequencies which are around few hundred Hz and few thousand Hz have been reported by various authors [6], [22],[20].

Figure 3-19 Kulite XTME-190

Conventional pressure transducers can not have high frequency responses as their diaphragms are located in a large cavity. Piezoresistive transducers are more suitable for unsteady pressure measurements. Kulite XTME 190 transducer which is shown in Figure 3-19 is used in this study. It is capable of measuring 17 bar (250) psi absolute pressure.

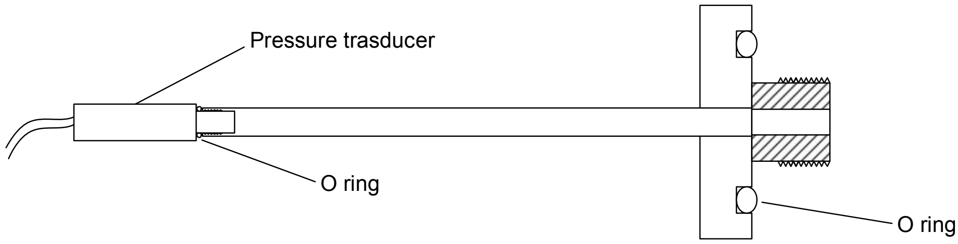

Figure 3-20 Pressure Sensor Assembly

The sensor has a very high (425 kHz) natural frequency which allows dynamic pressure measurements. It has an accuracy %1 of the full scale. Resolution of the sensor is infinitesimal and it can operate at temperatures up to 232ºC. As the combustor temperatures are higher, a thin and long tube is used between the combustor and pressure chamber. A sketch and a photo is given in Figure 3-20 and Figure 3-21 respectively.

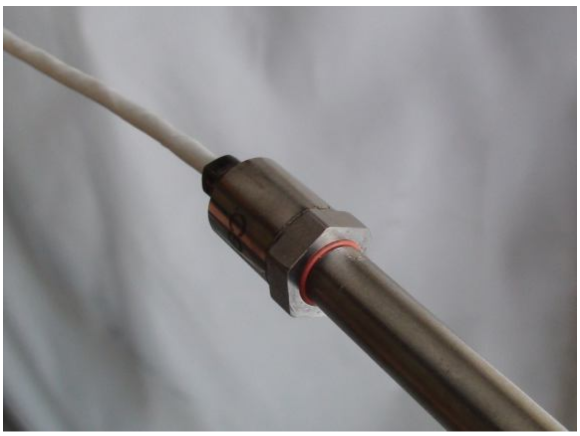

Figure 3-21 Pressure Sensor Mounted on the Combustor

The pressure sensor is a leadless design which allows it to operate at high temperatures.

3.4.3 Data Acquisition

Signals generated by thermocouple and pressure sensors are voltage differences. This voltage difference is very small and non linear in thermocouples.

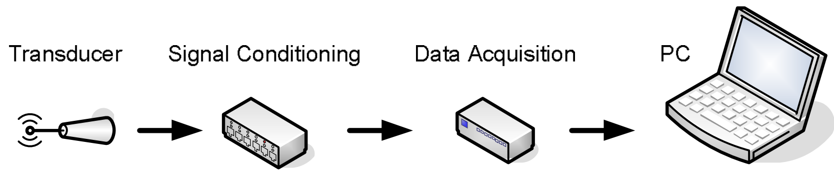

Figure 3-22 Data Acquisition Chain

Signal conditioning device linearizes and amplifies the voltage. Analog voltage signal is then digitized by data acquisition cards. The data is recorded in a computer hard disk. Data acquisition hardware used in this study are National Instrument USB data acquisition cards with 16 bit resolution. This means the analog signal is converted to digital with 2^{16} = 65536 levels. With a proper amplification, resolution of the signal is 0.0015% of its full scale which is better than measurement error of many transducers. This system is shown in Figure 3-23.

Figure 3-23 Signal Conditioning and Data Acquisition Box

R type thermocouples are standard; their calibration curves are defined in data acquisition system software. As tungsten rhenium thermocouples are manufactured specifically, calibration data is provided by manufacturers. A third order polynomial fit to manufacturer data is used for tungsten rhenium thermocouple signal conditioning. This polynomial is given in Figure 3-24.

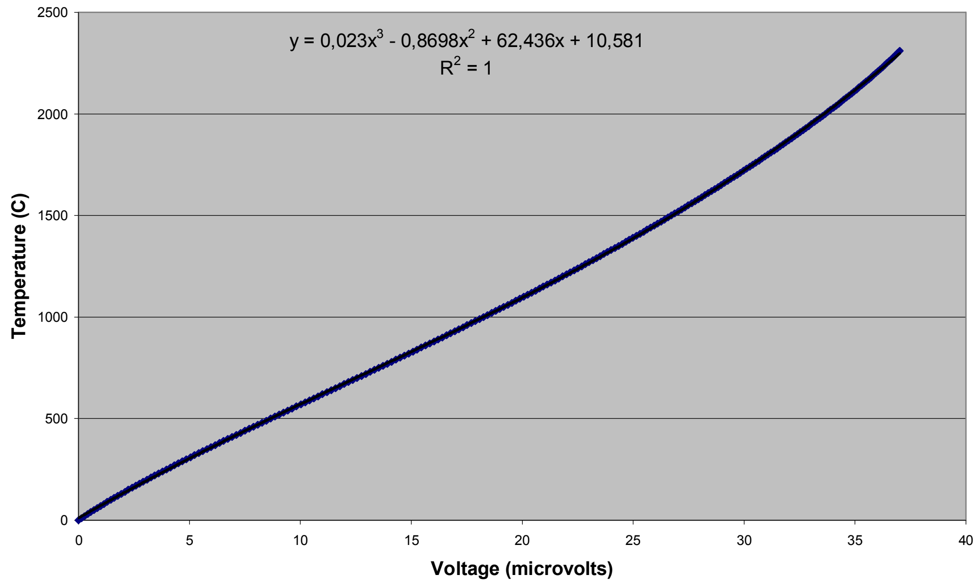

Figure 3-24 Calibration Curve of Tungsten Rhenium Thermocouple

A data acquisition software is prepared for the experiments by using National Instruments LabVIEW. While using the software, user can view the temperature and pressure measurements real-time both in graphs and in numeric indicators.

Signals are filtered by a 40 point moving average filter and have less significant figures in numeric indicators. After the test is completed, the gathered data can be viewed in charts. All of the measured values are in engineering units. They are converted to engineering units by calibration equations which can be changed before every test. Measurement data is also recorded in a text file.

User interface screen of the software is given in Figure 3-25. The block diagram is given in APPENDIX B.

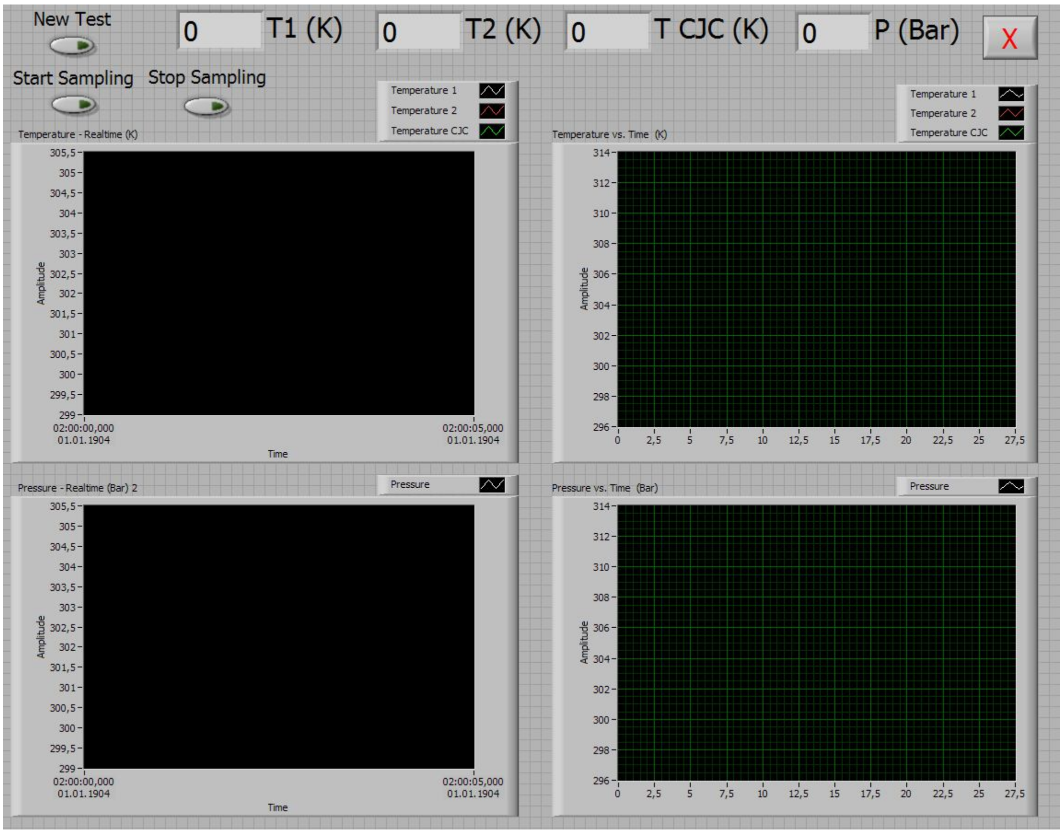

Figure 3-25 DAQ Software User Interface Screen

CHAPTER 4

DESIGN VERIFICATION OF THE TEST RIG

Design purpose of the test rig was stated as being able to perform experiments to compare combustion characteristics and combustion efficiency of different fuels and different fuel and air mixture ratios by making temperature and pressure measurements.

Cold flow experiments and four combustion experiments were performed for validation of the design of test rig and instrumentation. Hot gas products of fuel rich combustion of a hydrocarbon fuel is used in the experiments. The hot gas fuel was composed of hydrogen, carbon monoxide and other inert products.

4.1 EXPERIMENTS

Five reactive flow experiments, one without air flow, two oxidizer rich and one fuel rich case were conducted. First experiment was conducted to test if the structural elements of the rig and the instrumentation work properly at elevated temperatures. Three experiments are conducted in different air to fuel ratios. A fifth experiment is conducted for thermocouple dynamic behavior investigation.

Experiment cases are given in Table 4-1. Air to fuel ratios in air rich experiments are selected similar to the common examples in the literature. Fuel rich experiment was selected to have a higher non reacting mixture temperature.

Combustor geometry parameters air inlet angle and dome height are selected as 60º and 2H respectively. This configuration is used for the experiments as it was the combination with hottest dome region and most uniform exit temperature distribution.

Table 4-1 Experiment Cases

	Exp. 1	Exp. 2	Exp. 3	Exp. 4
Air inlet angle	60º	60º	60º	60º
Dome height	2H	2H	2H	2H
a/f	0	6.81	5.06	0.66
f/a	N/A	0.15	0.20	1.52
Equivalence Ratio	N/A	0.43	0.58	4.45
Test Duration	1.7s	1.7s	1.7s	1.7s
D_{th}	0.3H	0.3H	0.3H	0.3H

Conditions in which the experiments are conducted are given in Table 4-2.

Table 4-2 Experiment Conditions

	Exp. 1	Exp. 2	Exp. 3	Exp. 4
Pressure probe location	x=6.2H	x=6.2H	x=6.2H	x=6.2H
Temperature probe location	x=6.3H	x=6.3H	x=6.3H	x=6.3H x=3.2H
Data Acquisition Rate	10ks/s/ch	10ks/s/ch	10ks/s/ch	10ks/s/ch
Data Resolution	16 bit	16 bit	16 bit	16 bit
Ambient Pressure	897 kPa	897 kPa	897 kPa	905 kPa
Ambient Temperature	27 ºC	27 ºC	27 ºC	16 ºC
θ theoretical	N/A	1.74	1.64	1.12
θ of non reacting mixture	N/A	0.16	0.20	0.62
C* theoretical	N/A	1557 m/s	1609 m/s	2130 m/s
θ=Dimensionless Total Temperature $(T-T_{air})/(T_{fuel}-T_{air})$				

4.2 EXPERIMENTAL RESULTS

Results of the experiments are presented and analyzed in this section.

4.2.1 Cold Flow Experiment Results

Cold flow experiments are conducted to be able to supply constant pressure air to the test rig. Pressure time graph of the cold flow experiment which was conducted before the third experiment is shown in Figure 4-1. It is seen that constant pressure air can be supplied to the test rig.

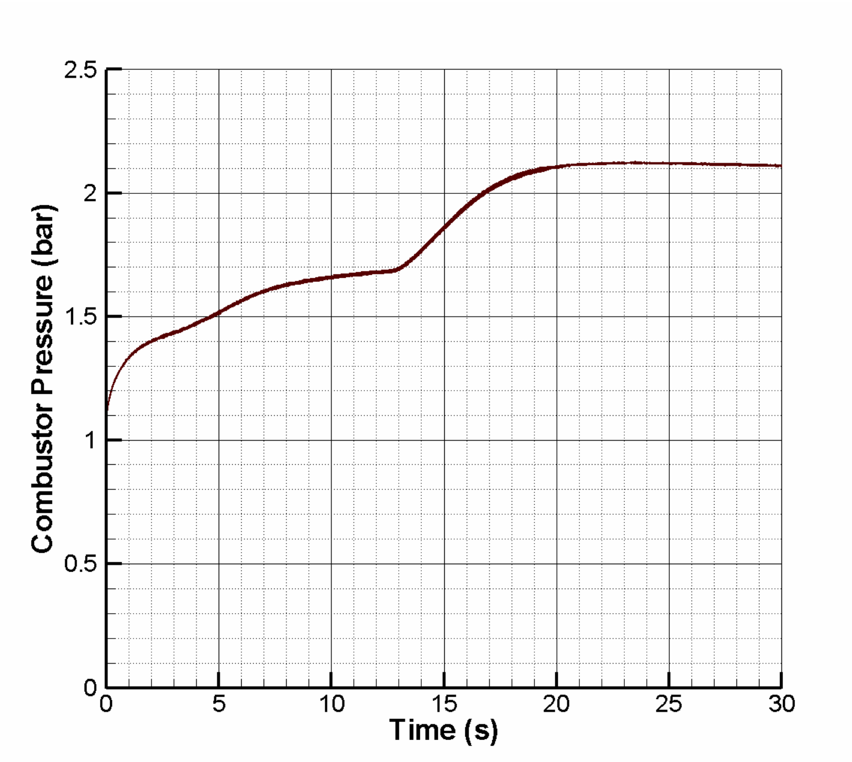

Figure 4-1 Cold Flow Experiment Pressure Time Graph

A CFD simulation at the experimental condition is conducted. Figure 4-2 shows the pressure distribution in the combustor nozzle at t=30s. By these experiments and simulations, discharge coefficient of the combustor nozzle is found to be 0.8.

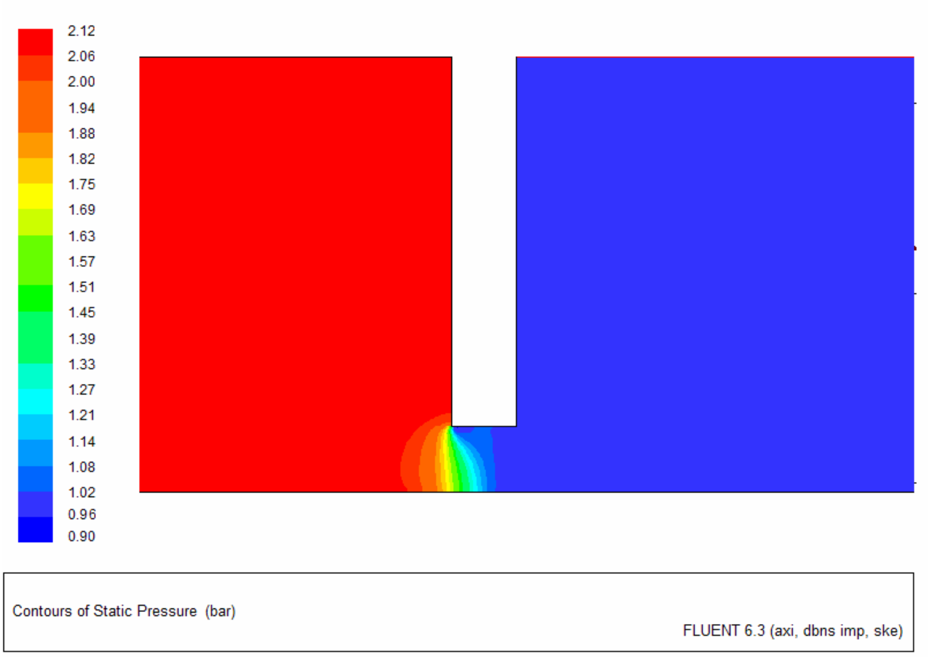

Figure 4-2 Pressure Distrubution in Combustor Nozzle in Cold Flow Experiment

In cold flow simulations, FLUENT commercial sowtware is used as better convergence is achieved in two dimensional axissymetric nozzle flow.

4.2.2 Measurement Results

Temperature and high frequency pressure data are gathered. Also high speed camera images are recorded.

4.2.2.1 Temperature Measurements

Thermocouples are measurement devices with a first order dynamic behavior. Dimensionless total temperature vs. time graph of temperature at first experiment is given in Table 4-1. The continuous rise up to 1.7 seconds represents a step response of a first order system. Decrease in temperature afterwards is due to the continuing air flow after fuel flow is stopped.

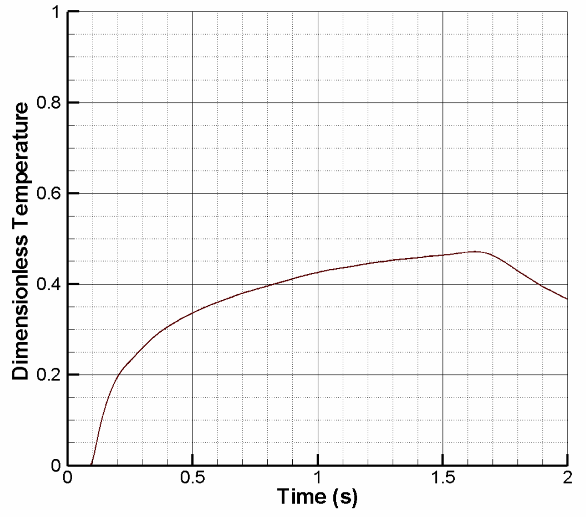

Figure 4-3 Temperature Measurement From Combustor in Experiment 1

Dimensionless temperature vs. time graph of temperature at second experiment is given in Figure 4-4. It is observed that temperature rises in five steps. First of these steps is the start of fuel feed at time equal to 0.2 s. The remaining four steps are located 0.6, 0.9, 1.1 and 1.3 s after the first step.

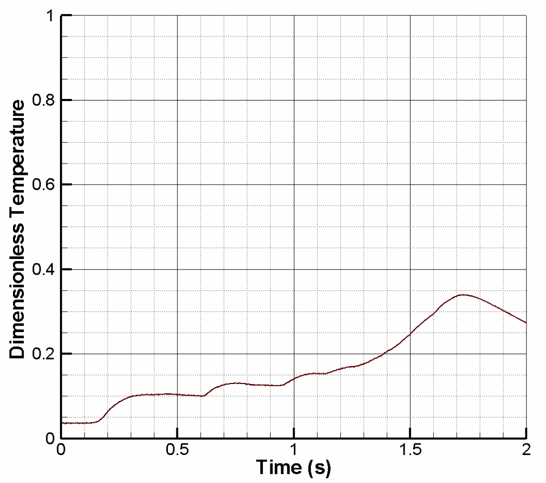

Figure 4-4 Temperature Measurement From Combustor in Experiment 2

In Figure 4-5, dimensionless temperature vs. time graph of third experiment is given. Similar to the case of first experiment step response of a first order system is observed.

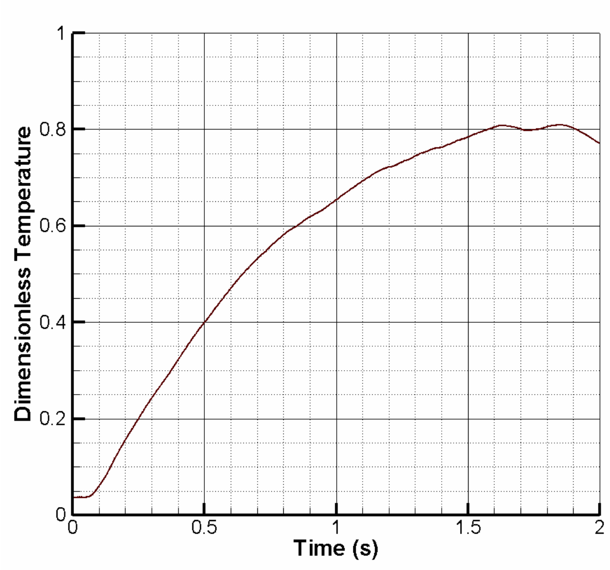

Figure 4-5 Temperature Measurement From Combustor in Experiment 3

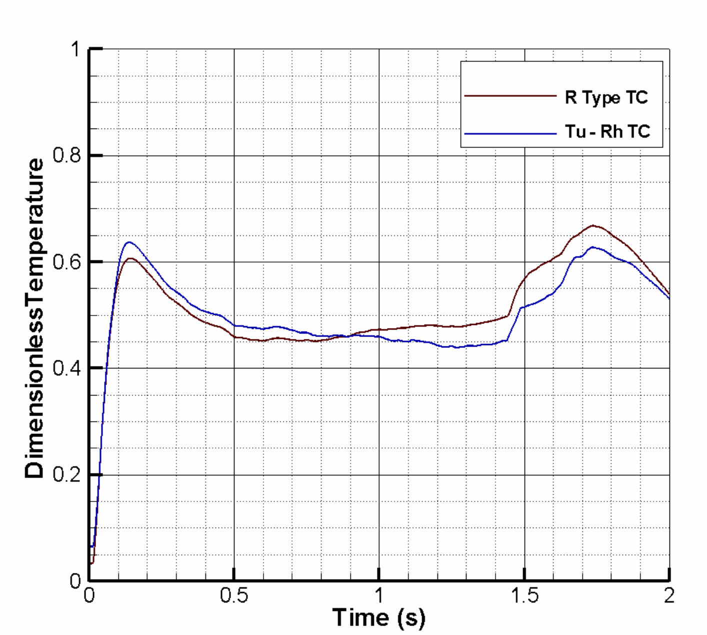

Figure 4-6 Temperature Measurement in Experiment 4 (x=6.3H)

In Figure 4-6 and Figure 4-7 temperature measurements at positions x=6.3H and x=3.2H are given respectively. A quicker time response is observed in these measurements. An improved probe design where smaller (0.1 mm) thermocouple junction wires were used yielded into a lower time constant. A slight increase in the temperature is seen during the last 0.2 s of the test.

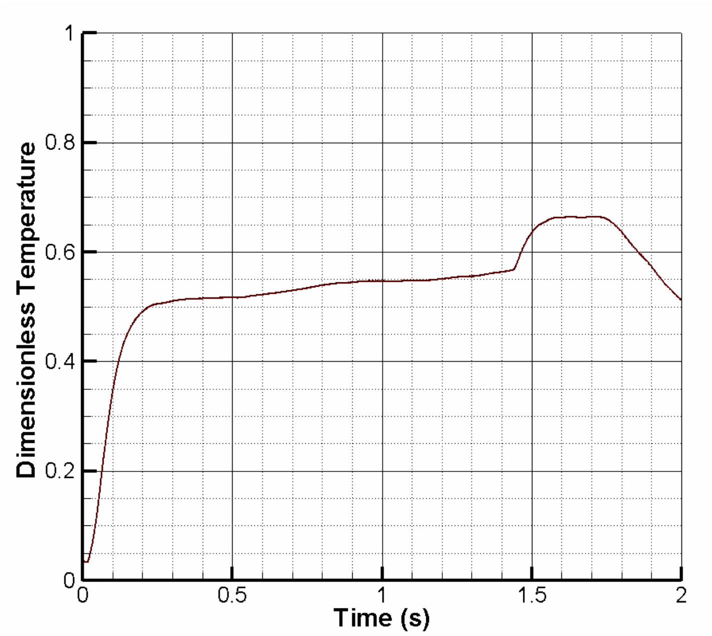

Figure 4-7 Temperature Measurement in Experiment 4 (x=3.2H)

Using thinner thermocouple wires has resulted in quicker temperature measurements. Time responses of these thermocouples are investigated by a fifth experiment. In this experiment, infrared (IR) camera images were recorded. Temperature measurements by thermocouples and IR thermometry are compared in Figure 4-8. Although thermocouples are not quick enough to resolve the peak at the start, their time response is better than the ones in first three experiments. Two IR camera images, at t=0.1 and t=1.0 are given in Figure 4-9.

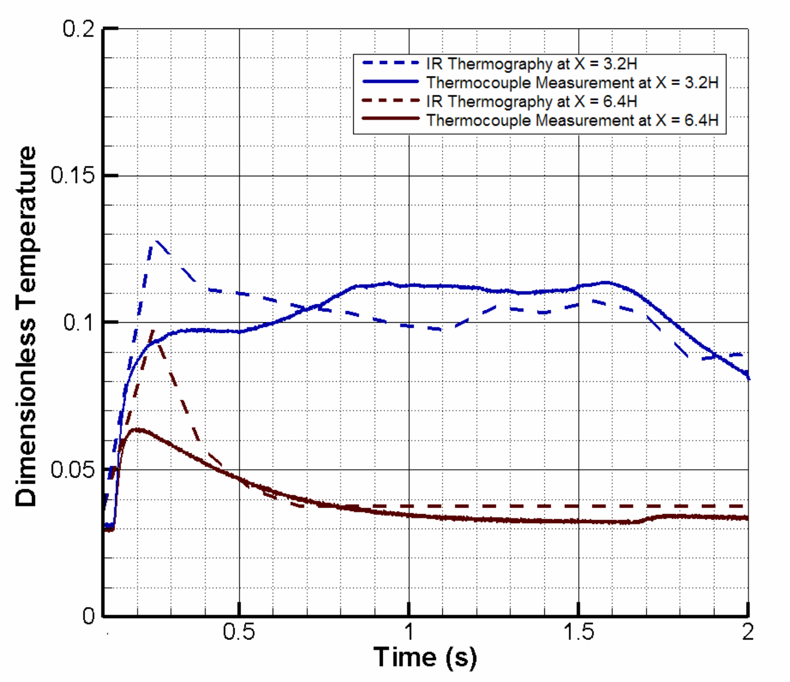

Figure 4-8 Thermocouple Measurements vs IR Thermometry

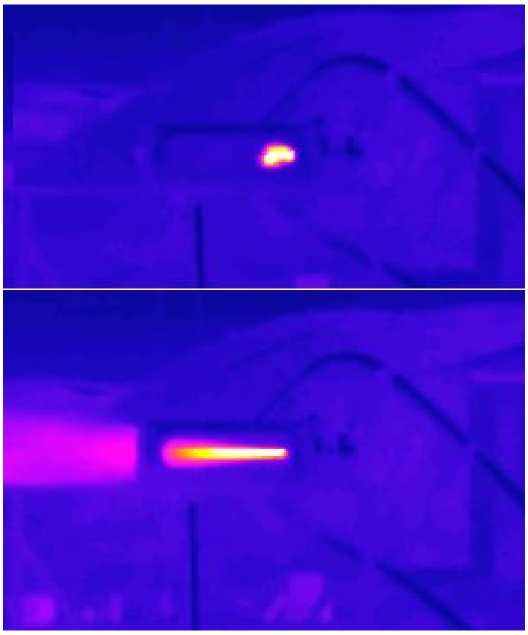

Figure 4-9 IR Thermal Camera Images (up t=0.1s, below t=1.0s)

4.2.2.2 Pressure Measurements

Pressure data is gathered from the combustor in four experiments. In Figure 4-10 pressure measurements of the first experiment is given. Only a slight increase occurs as there is no air feed.

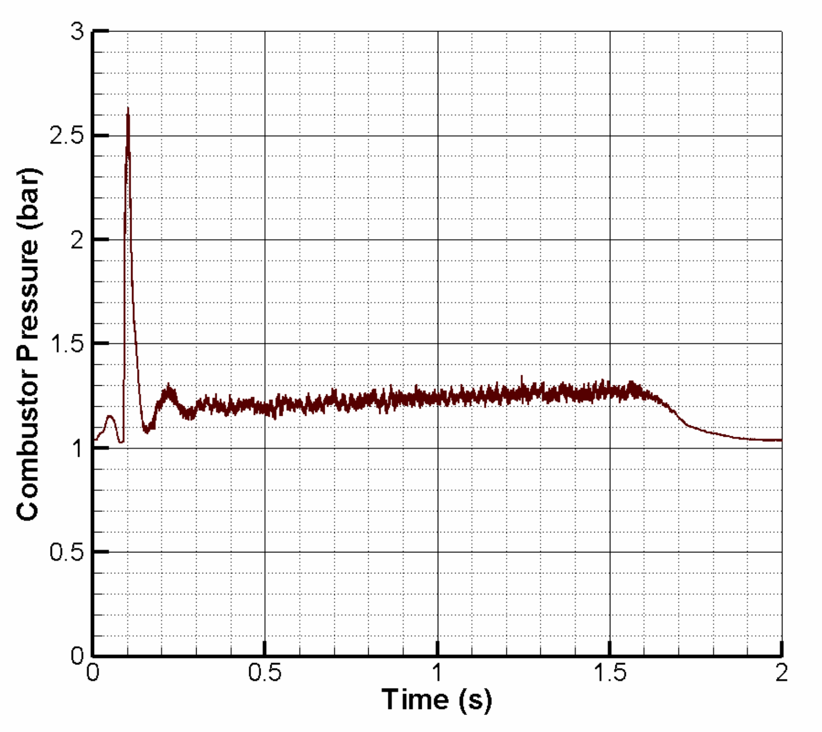

Figure 4-10 Combustor Pressure in Experiment 1

Pressure measurement results of second experiment are given in Figure 4-11. Jumps of pressure are observed at certain moments. Pressure jumps are located at the same moments with the increases in temperature measurements of second experiment. In Figure 4-12 a fluctuating pressure during the third experiment is observed. Pressure measurement of fourth experiment is given in Figure 4-13. A slight increase in pressure and fluctuations are present at the last 0.2 s of the experiment.

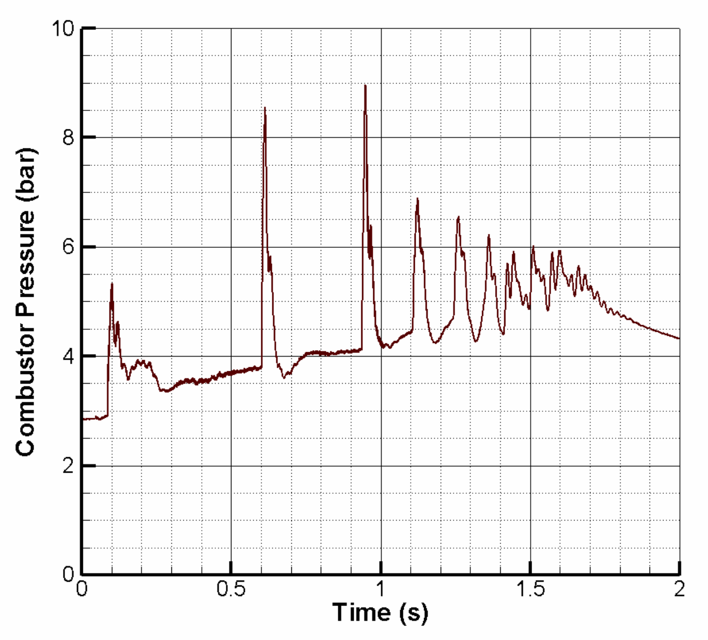

Figure 4-11 Combustor Pressure at Experiment 2

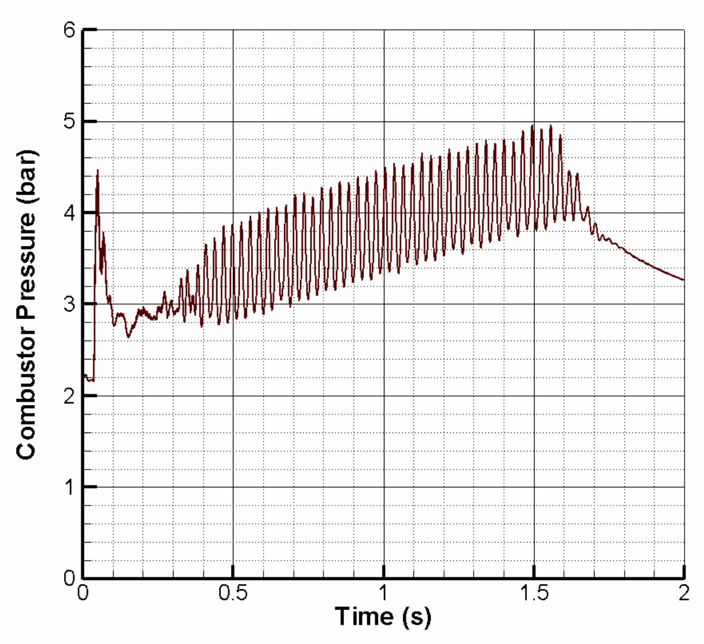

Figure 4-12 Combustor Pressure at Experiment 3

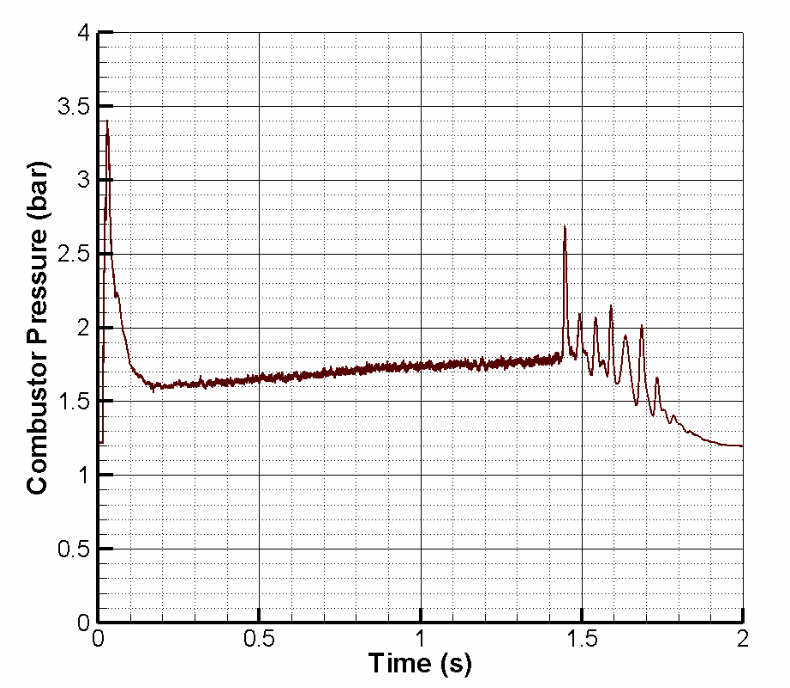

Figure 4-13 Combustor Pressure at Experiment 4

4.2.2.3 Flow Visualization

Combustion is visualized by high speed camera recordings. Images were recorded at 1000 frame per seconds (fps). High speed camera images of the first, second and third experiments are given in Figure 4-14, Figure 4-15 and Figure 4-16 respectively. Images given in the report are reduced to 20 fps and 25 fps. I

n the first experiment, flame was too bright so sensor of the camera was saturated. In the second experiment, diaphragm of the camera was closed another stop which reduced the saturation but was not enough to prevent it completely. In the third experiment, diaphragm of the camera was closed four more stops. Hence, images were recorded without saturation.

Figure 4-14 High Speed Camera Images of Experiment 1 (20 fps)

Figure 4-15 High Speed Camera Images of Experiment 2 (20 fps)

Figure 4-16 High Speed Camera Images of Experiment 3 (25 fps)

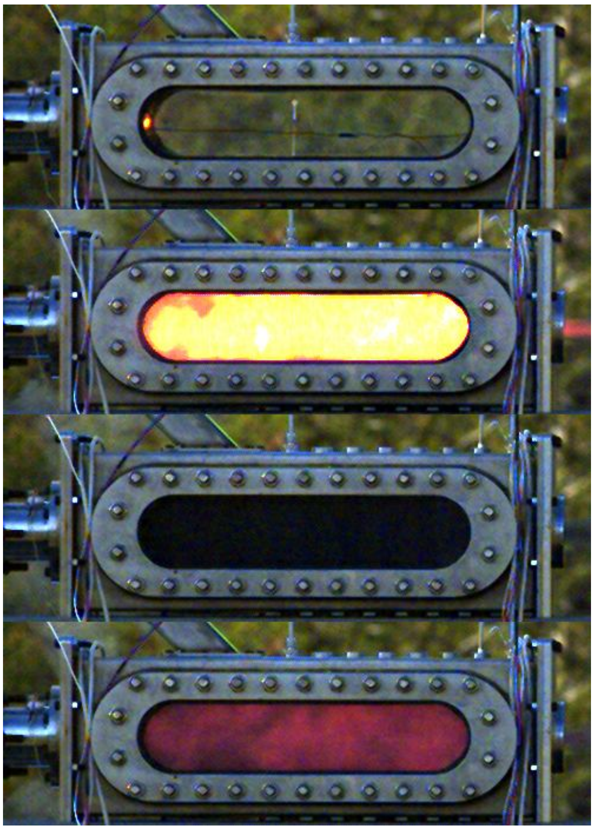

Figure 4-17 High Speed Camera Images of Experiment 4

In the first two experiments, image was too bright to see the details of the combustion. In experiment three it was seen that flame was appearing and vanishing periodically. Phase and frequency of this was compatible with the fluctuations in the pressure measurements. On fourth experiment, a black smoke was observed until the last 0.2 seconds.

4.2.3 Evaluation of Measurement Results

The step responses of thermocouples in first three experiments were analyzed by the method proposed for aspirated thermocouple probes in reference [35] and [36]. This analysis was not performed for fourth experiment as time response was quick enough.

An exponential curve was fit to the temperature data by using curve fitting toolbox of MATLAB. Exponential fit and the data is given in Figure 4-18

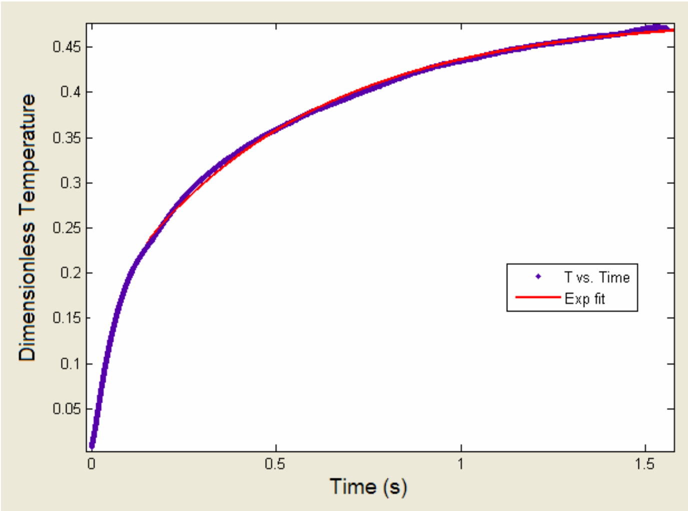

Figure 4-18 Exponential Curve Fit to Temperature Data of Experiment 1

In Figure 4-19 it is seen that when extrapolated, curve fit reaches a value asymptotically.

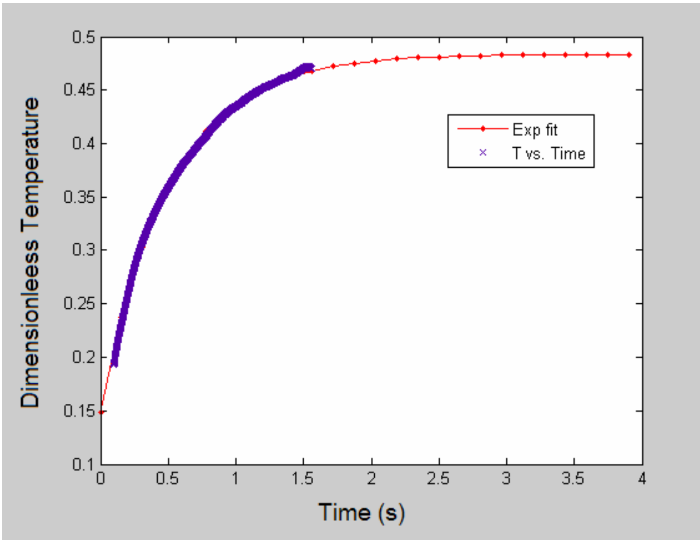

Figure 4-19 Extended Exponential Fit to Temperature Data in Experiment 1

A model equation with the form of “f(x) = a*exp(-b*x)+c” was generated by using MATLAB curve fitting toolbox. c is the value which the curve fit reaches asymptotically. Hence c is the value of the step input to the first order system. Coefficients of the model equation for the first experiment are given in Table 4-3.

Table 4-3 Model Equation for Experiment 1

Model equation	f(x) = a·exp(-bx)+c
Coefficients (with 95% confidence bounds)	a = -0.3346 (-0.3349, -0.3343)
	b = 1.962 (1.957, 1.967)
	c = 0.4837 (0.4835, 0.4839)
Goodness of fit	R-square= 0.9977

Exponential curve was fit to the last rise in temperature data of the second experiment. This curve fit is given in Figure 4-20.

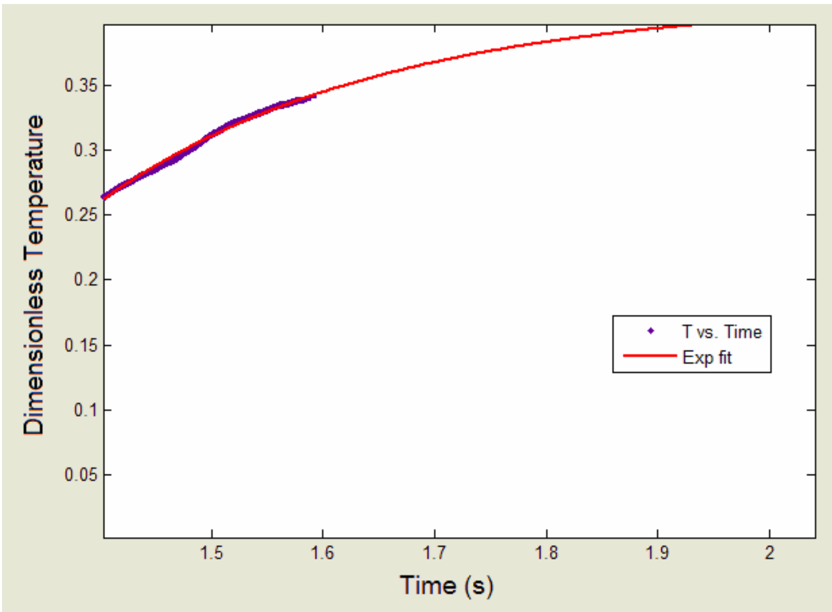

Figure 4-20 Exponential Curve Fit to Temperature Data of Experiment 2

Coefficients of the model equation for the second experiment are given in Table 4-4.

Table 4-4 Model Equation for Experiment 2

Model equation	f(x) = a·exp(-bx)+c
Coefficients (with 95% confidence bounds)	a = -39.29 (-46.03, -32.55)
	b = 3.953 (3.814, 4.091)
	c = 0.4149 (0.4112, 0.4187)
Goodness of fit	R-square= 0.9936

Table 4-5 Model Equation for Experiment 3

Model equation	f(x) = a·exp(-bx)+c
Coefficients (with 95% confidence bounds)	a = -0.9848 (-0.9854, -0.9842)
	b = 1.424 (1.421, 1.427)
	c = 0.9062 (0.9057, 0.9067)
Goodness of fit	R-square= 0.9995

Curve fit of third experiment and model equation parameters are given in Figure 4-21 and Table 4-5 respectively.

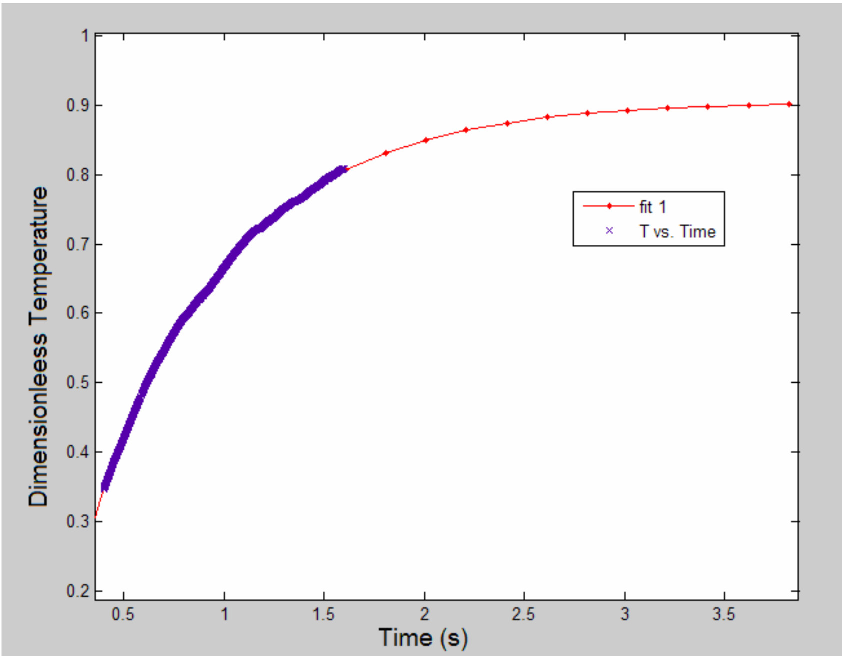

Figure 4-21 Exponential Curve Fit to Temperature Data of Experiment 3

Pressure fluctuations were observed in second and third experiments. Also pressure fluctuations were present at the last 0.2 s of the fourth experiment. Frequencies of these pressure fluctuations were found by a Fast Fourier Transform analysis.

Fast Fourier Transformation of the data was done in MATLAB by using the commands given in Table 4-6.

Table 4-6 MATLAB Commands for Fast Fourier Transform

```
Y = fft(P);
Y(1)=[];
n=length(Y);
power = abs(Y(1:floor(n/2))).^2;
nyquist = 1/2;
daqrate = 10000;
freq = (1:n/2)/(n/2)*nyquist*daqrate;
plot(freq,power)
xlabel('Hz')
title('Power Spectra')
plot(freq(1:100),power(1:100))
xlabel('Hz')
```

Frequency spectrums of pressure fluctuations in second, third and fourth experiments are given in Figure 4-22, Figure 4-23 and Figure 4-24 respectively.

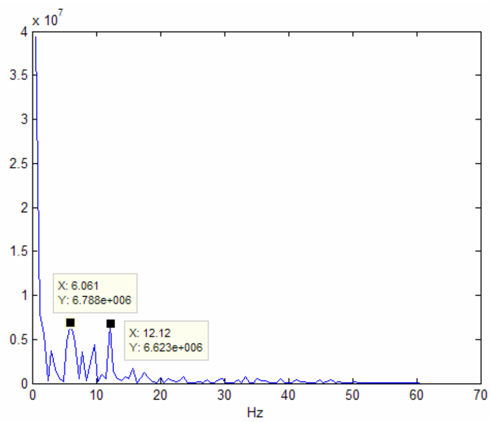

Figure 4-22 Pressure Fluctuation Frequency Spectrum of Experiment 2

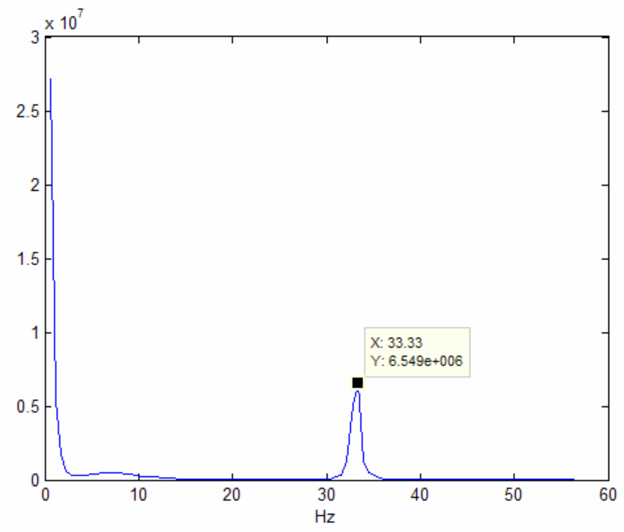

Figure 4-23 Pressure Fluctuation Frequency Spectrum of Experiment 3

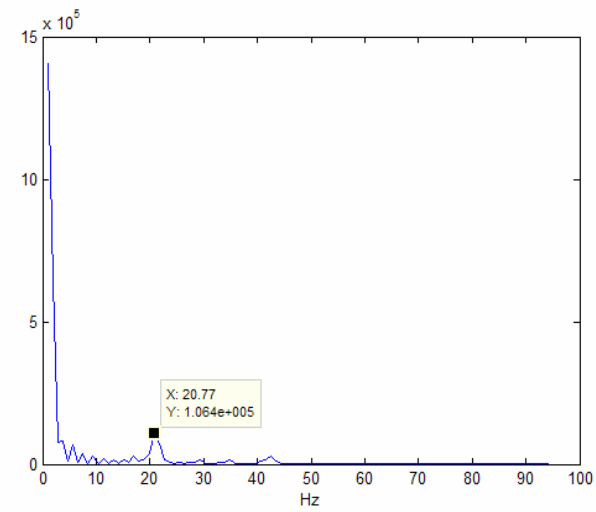

Figure 4-24 Pressure Fluctuation Frequency Spectrum of Experiment 4

Helmholtz frequency in a cavity is defined as

$$F_H = \frac{a}{2\pi}\sqrt{\frac{A_{neck}}{V_{cavity}L_{cavity}}} \tag{4.1}$$

For a pipe with constant cross section area it is reduced to

$$F_H = \frac{a}{2\pi L} \tag{4.2}$$

For the 0.8 meter long pipe which connects the pressure transducer to the combustor, Helmholtz frequency is 68 Hz. Hence the pressure oscillation frequencies are not resonant with pipe Helmholtz frequency.

4.2.4 Interpretation of the Results

First experiment showed that mechanical elements of the test rig were working properly at high temperature conditions. Specially designed gaskets were not leaking, quartz windows were resistant to high temperature differences between their surfaces and no abrasion was observed in fuel supply and combustor orifices.

Table 4-7 Experiment Results

	Exp. 1	Exp. 2	Exp. 3	Exp.4
f/a	N/A	0.15	0.20	1.52
a/f	0	6.81	5.06	0.66
Equivalence Ratio	N/A	0.43	0.58	4.45
η_{c*}(%)	N/A	24	55	58
η_T (%)	N/A	33	39	49
Mean Pressure (bar)	1.2	4.1	3.8	1.8
θ Combustor	0.48	0.42	0.91	0.65
θ theoretical	N/A	1.74	1.64	1.12
θ of non reacting mixture	N/A	0.16	0.20	0.62
Pressure Fluctuation Rate (Hz)	N/A	12	33	21
θ =Dimensionless Total Temperature $(T-T_{air})/(T_{fuel}-T_{air})$				

Quantitative results of the experiments are presented in Table 4-7. Combustor efficiency based on temperature rise is calculated by using thermocouple measurements. C* efficiencies are calculated by using mean pressure measurements.

For experimental determination of C*, nozzle discharge coefficient is also needed. In AGARD Report 323, it is stated that experimental determination of discharge coefficient is usually not practical as very accurate simultaneous pressure, mass flow rate and temperature measurements are needed. It is suggested that discharge coefficients to be found theoretically [30]. CFD simulations at experimental conditions were made for nozzle discharge coefficient determination. These values were used in C* efficiency calculations. In experiment 2, exponential curve fit to temperature was generated with less data as temperature rise did not have first order step response characteristics throughout the experiment. This resulted in a poor prediction of combustor temperature and thermal efficiency in the second experiment. Hence C* efficiency is a better measure when flame is not stable.

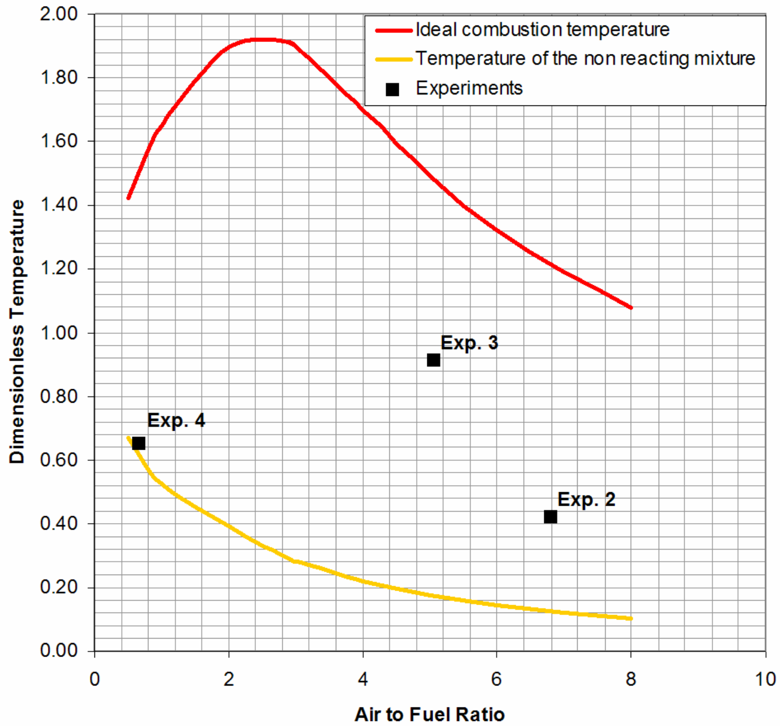

Figure 4-25 Combustor Temperatures in Experiments

Combustor temperatures are compared to non adiabatic mixture temperature and ideal combustion temperature in Figure 4-25. In second and third experiments, combustion occurs whereas air is heated by the high temperature fuel without combustion in fourth experiment. It is seen that Experiment 2 has the lowest thermal efficiency. Temperature has risen in certain moments during the experiment. The rise in temperature was also coupled by rapid and short term increases in pressure. This means that the flame is not stable and it vanishes during the experiment. When the pressure fluctuations and temperature rise in second experiment are investigated together, it is seen that there is a step rise in temperature corresponding to each pressure jump. A flame is formed at every pressure jump and it vanished by cooling of cold combustor environment.

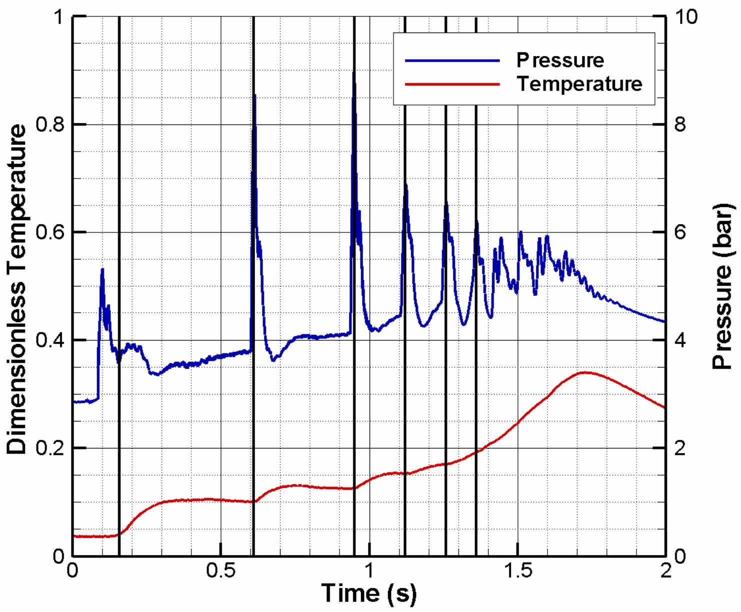

Figure 4-26 Pressure and Temperature Measurements in Experiment 2

Shoji studied effects of non reacting air and combustor temperature on ignition and formation of a flame. In Figure 4-27, the regions of stable flame formation are given. Shoji used a solid fuel gas generator as the hot fuel source. Hence the combustion in the gas generator is defined as primary flame and the flame inside the test combustor is defined as secondary flame. Shoji describes a limiting temperature for a secondary flame. [25].

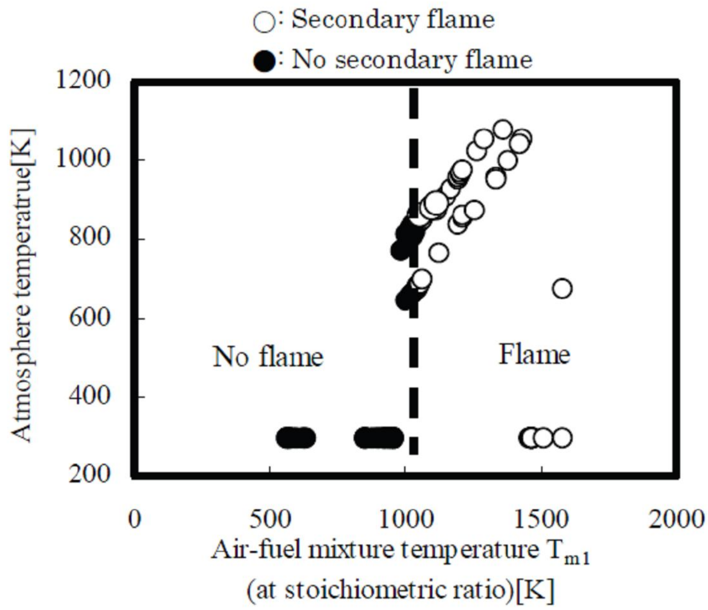

Figure 4-27 Formation of the Secondary Flame [25]

Similarly, the flame was not stable in air rich experiments. The reason is probably low combustor temperature which could not sustain the flame.

Third experiment which has a greater non reacting mixture temperature as the air to fuel ratio is lower, had a more stable flame and greater combustion efficiency then the second experiment. This resulted in a continuous rise in temperature measurement and a better efficiency. Pressure fluctuations were present also in the third experiment. High speed camera images showed flame brightness and length changes at the same frequency and phase with pressure fluctuations.

Finally a fuel rich case was investigated in fourth experiment. Purpose was to have a higher mixture temperature at the beginning. This experiment had a better thermal and C* efficiency. However this was because of the fact that experiment had the lowest ideal combustor temperature as all of the fuel can not be burned completely. This resulted in a higher efficiency although the combustor temperature was slightly above the non reactive mixture temperature. An ignition delay was present in this experiment due to the lack of oxygen. Flame was observed at the last 0.2 seconds of the experiment by high speed camera images. Temperature was also slightly increased. This resulted as the fuel rate was lowered gradually at the end of the test. Air to fuel ratio at this last 0.2 second period was greater than the initial value in the experiment. In this experiment, thermocouple wires with quicker response (0.1 mm junction size) were used. Hence temperature rise in the last 0.2s in the test could have been resolved by temperature measurements.

In the fifth experiment, by comparing to IR thermography measurements, it was seen that 0.1 mm junction sized thermocouple dynamic response was quick enough to resolve temperature changes in the combustor.

CHAPTER 5

CONCLUSION AND DISCUSSION

One of the most crucial technological challenges in air breathing propulsion is to design efficient, reliable and robust combustion chambers. Motivation of this study was to achieve a method to have a deeper understanding of air breathing rocket combustors. As a result of a detailed literature survey, it was seen that investigation of different fuel compositions and different air to fuel ratios by using scaled combustors was a common and valuable method.

In this thesis, a combustion test rig which can be used for investigation of combustion efficiency and flame structure of different fuels and different air to fuel ratio conditions in air breathing rockets was developed. Parameters required to be measured for efficiency calculation and combustion investigation were determined. The test rig design was originated to satisfy these measurement requirements.

By the CFD simulations of the reactive flow, which were done for ballistic design of the test rig, it was seen that the combustor cross section was large enough to investigate different air to fuel ratios with minor effect from flow field. Analysis of simulation results showed that combustion efficiency was much more sensitive to air to fuel ratio compared to the geometrical parameters. Temperature and pressure probe locations, where velocities should be close to zero and temperature should be close to mean combustor outlet temperature was also selected as a result of CFD simulations.

A reactive flow experiment was conducted for testing the mechanical design of the scaled combustor. By this experiment it was seen that specially designed gaskets were able to prevent leakages at elevated temperatures during the tests. Quartz windows could also withstand the high temperature and thermal gradient at the tests. Also it was seen that the measurements could be done at high temperatures. AISI 310 stainless steel combustor was used without corrosion problem in the experiments.

Four reactive flow experiments were conducted at different fuel to air ratios with both oxidizer and fuel rich configurations. A separate fifth experiment was conducted for thermocouple dynamic behavior investigation. During the experiments, temperature, pressure and flow field images were gathered. Infrared thermography, thermocouples with platinum, tungsten and rhenium materials were used for combustor temperature measurements. It was seen that dynamic response of the 0.2 mm thermocouples was not enough to resolve temperature rise during the experiment. Exponential curve fitting was used for temperature calculation. However temperature changes of the combustor when the flame was not stable could not be resolved by 0.2 mm thermocouples. Dynamic response of 0.1 mm junction thermocouples was observed by IR thermography. Although they need to be replaced more frequently because of the degradation, thermocouple wires with 0.1 mm junction were preferable as their dynamic response was much better. Oscillating pressure measurements were gathered by high temperature piezoresistive pressure sensors with high frequency response. Pressure fluctuations were observed. Frequency of the pressure fluctuations were compared high speed cameras recordings through the quartz windows. It was seen that pressure fluctuations had the same frequency with the changes in flame brightness and length.

It was seen that flames in the air rich cases were not stable due to the low combustor temperatures. The cooling rate by mixing exceeded the heating rate by reaction. Efficiency increase with increasing fuel to air ratio at air rich experiments was observed. This was due to higher combustor temperatures at higher fuel to air ratios.

The fuel rich case had an ignition delay. Flame was present in the last 0.2 seconds of the test. Fuel rich experiment had the lowest ideal combustor temperature as all of the fuel can not be burned even in ideal conditions. Hence efficiency of this case was higher than the air rich cases although combustor temperature was slightly above the non reactive mixture temperature.

As a conclusion, it was seen that the combustion test rig which is developed in this study is capable of examining the flame structures and combustion efficiency of different fuel and air to fuel mixtures for air breathing rocket combustor studies.

REFERENCES

[1] Schadow K., *"Experimental Investigation of Boron Combustion in Air Augmanted Rockets"*, AIAA Journal, Vol.7, No.10, October 1969."

[2] Schadow K., *"Study of Gas-Phase Reactions in Particle-Laden, Ducted Flows",* AIAA Journal, Vol.11, No.7, July 1973.

[3] Abbot S.W., Smoot L.D., and Schadow K., *"Direct Mixing and Combustion Efficiency Measurements in Ducted, Particle-Laden Jets"* AIAA Journal Vol.12, No.3, March 1974.

[4] Schadow K., *"Fuel-Rich Particle-Laden Plume Combustion"* AIAA Journal, Vol.13, No.12, December 1975.

[5] Clark, W.H., *"Experimental Investigation of Pressure Oscillations in a Side Dump Ramjet Combustor"*, Journal of Spacecraft and Rockets, Vol. 19, No. 1, pp 47-53, January-February 1982.

[6] Crump J.E., Schadow K.C., Yang V., and Culick F.E.C., *"Longitudinal Combustion Instabilities in Ramjet Engines: Identification of Acoustic Modes",* Journal of Propulsion, Vol.2, No.2, Merch-April 1986.

[7] Liou T.M. and Wu S.M., *"Flowfield in a Dual-Inlet Side-Dump Combustor"*, Journal of Propulsion, Vol.4, No.1, January-February 1988.

[8] Cherng D.L., Yang V. and Kuo K.K. *"Numerical Study of Turbulent Reacting Flows in Solid- Propellant Ducted Rocket Combustors"*, Journal of Propulsion, Vol.5, No.6, November-December 1989.

[9] Stull, F.D., Craig, R.R., Streby, GD., and Vanka, S.P., *"Investigation of a Dual Inlet Side Dump Combustor Using Liquid Fuel Injection"*, AIAA paper AIAA-83-0420, AIAA 21st Aerospace Sciences Meeting, Reno, Nevada, US., 10-13 January 1983.

[10] Vanka S.P., Craig R.R. and Stull F.D., “Mixing, Chemical Reaction, and Flowfield Development in Ducted Rockets”, Journal of Propulsion, Vol.2, No.4, July-August 1986.

[11] Schadow K.C., Wilson K.J., Lee M.J. and Gutmark E., *“Enhancement of Mixing in Reacting Fuel-Rich Plumes Issued from Elliptical Nozzles”*, Journal of Propulsion, Vol.3, No.2, March-April 1987.

[12] Schadow K.C., Gutmark E., Wilson K.J. and Parr D.M. *“Mixing Characteristics of a Ducted Elliptical Jet”*, Journal Of Propulsion, Vol.4, No.4, July-August 1988.

[13] Gutmark E., Schadow K.C. and Wilson K.J., “Subsonic and Supersonic Combustion Using Noncircular Injectors”, Journal of Propulsion, Vol.7, No.2, March-April 1991.

[14] Schadow K.C., Gutmark E., Parr T.P., Parr D.M., Wilson K.J. and Ferrel G.B., *“Enhancement of Fine-Scale Turbulence for Improving Fuel-Rich Plume Combustion”,* Journal of Propulsion, Vol.6, No.4, July-August 1990.

[15] Schadow K.C., Gutmark E., Wilson K.J., and Smith R.A., “Multistep Dump Combustor Design to Reduce Combustion Instabilities”, Journal of Propulsion, Vol.6 ,No.4, July-August 1990.

[16] Ajdari E., Gutmark E., Parr T.P., Wilson K.J. and Schadow K.C. “Thermal Imaging of Afterburning Plumes” Vol.7, No.6, November-December 1991.

[17] Albagli D. and Levy Y., “Experimental Study on Confined Two-Phase Jets” Journal of Thermophysics, Vol.5, No.3, July-September 1991.

[18] Dijkstra, F., Mayer, A.E.H.J., Smith, R.A., Wilson, K.J., and Schadow, K.C., "Ducted Rocket Combustion Experiments at Low Gas Generator Combustion Temperatures", AIAA paper AIAA-95-2415, AIAA/ASME/SAE/ASEE 31st Joint Propulsion Conference, San Diego, California, U.S., 10-12 Jdy 1995.

[19] Stowe R., "Performance Prediction of a Ducted Rocket Combustor", Ph.D. Thesis, l'Université Laval, 2002, Québec, Canada.

[20] Stowe R.A., Dubois C., Harris P.G., Mayer A.E.H.J., deChamplain A. and Ringuette S., "Performance Prediction of a Ducted Rocket Combustor Using a Simulated Solid Fuel", Journal of Propulsion and Power, Vol.20, No.5, September-October 2004.

[21] Brophy C.M. and Hawk C.W., "Mixing and Combustion Studies of Four Inlet Side Dump Combustors", AIAA paper AIAA 96-2765, 32nd AIAA/ASME/SAE/ASEE Joint Propulsion Conference, July 1-3, 1996, Florida.

[22] Wilson K.J., Gutmark E., Schadow K.C., and Smith R.A., "Feedback Control of a Dump Combustor with Fuel Modulation", Journal of Propulsion and Power, Vol.11, No.2, March-April 1995

[23] Ristori A. and Cochet A., "Research ramjet program: an initiative to improve knowledge on ramjet reactive flowfields", 4th ONERA/DLR Aerospace Symosium, 13-14January 2002, Cologne

[24] Ristori A., Reichstadt S., Brossard C. and Heid G., "PIV and gas sampling analysis measurements for fuel-to-air mixing study inside a research ramjet combustor", ISFV13 - 13th International Symposium on Flow Visualization, July 1-4, 2008, Nice, France

[25] Miyayama T., Oshima H., Toshiyuki S., Odawara T., Tanabe M. and Kuwahara T., "Improving Combustion of Boron Particles in Secondary Combustor of Ducted Rockets", 42nd AIAA/ASME/SAE/ASEE Joint Propulsion Conference & Exhibit, 9-12 July 2006, Sacramento

[26] Shoji T., Tanabe M. and Kuwahara T., "Jet Flame Characteristics in the Secondary Combustor of Ducted Rockets", 42nd AIAA/ASME/SAE/ASEE Joint Propulsion Conference & Exhibit, 9-12 July 2006, Sacramento

[27] ARKUN U.O., "Design and production of a Liquid Propellant Ramjet", M.Sc. Thesis, METU, 1993, Ankara.

[28] Sutton, G., P., Biblarz, O., *"Rocket Propulsion Elements"*, John Wiley & Sons, 7th edition, 2001,

[29] Mattingly, J.D., *"Elements of propulsion: gas turbines and rockets"*, AIAA Education Series, 2006.

[30] AGARD Advisory Report 323, "Experimental and Analytical Methods for the Determination of Connected-Pipe Ramjet and Ducted Rocket Internal Performance", July 1994.

[31] Gordon S. and McBride B.J., "Computer Program for Calculation of Complex Chemical Equilibrium Compositions, Rocket Performance, Incident and Reflected Shocks, and Chapman-Jouguet Detonations", NASA-SP-273, Interim Revision, March 1976.

[33] Star CCM User Manual , 2006, www.cd-adapco.com

[34] Box G.E.P., Hunter J.S. and Hunter G.W., *"Statistics for Experimenters An Inteoduction to Design, Data Analysis and Model Building"* Wiley and Sons, 2nd Edition, 1978, New York.

[35] Brouckaert J.F., "Advanced High Temperature Insstrumentation for Gas Turbine Applications" VKI Lecture Series 2009-6

[36] Van den Braembussche R.A. et. al., "Measurement Techniques in Fluid Dynamics, An Introduction" VKI Lecture Series 1994-01, 2nd revised edition. "

APPENDIX A

SAMPLE ANOVA CALCULATION

Hata! Yer işareti başvurusu geçersiz. summarizes the results that will be used in analysis of variance calculations.

Table A-1 Summary of Responses

	j: Dome Height (B)			
	0.5H		1H	
	k: f/a (C)		k: f/a (C)	
i: Angle (A)	0.15	0.30	0.15	0.30
45	0.84	0.94	0.83	0.93
60	0.87	0.93	0.87	0.94

For preparation of Analysis of Variance (ANOVA) table square of sums are calculated by using following expressions. M, K and L are factor levels of parameters A, B and C. n is the number of replications. T_{ijk} is the sum of responses where i,j and k are indices of parameters A, B, and C. Using square of sums ANOVA table is constructed as given in Table A-2.

$$SS_T = \sum_{i=1}^{M} \sum_{j=1}^{K} \sum_{k=1}^{L} \sum_{l=1}^{n} X_{ijkl}{}^2 - \frac{T_{...}{}^2}{MKLn} \quad dof_T = MKLn - 1$$

$$SS_A = \sum_{i=1}^{M} \frac{T_{i..}{}^2}{KLn} - \frac{T_{...}{}^2}{MKLn} \quad dof_A = M - 1$$

$$SS_B = \sum_{j=1}^{K} \frac{T_{.j.}{}^2}{MLn} - \frac{T_{...}{}^2}{MKLn} \quad dof_B = K - 1$$

$$SS_C = \sum_{k=1}^{L} \frac{T_{..k}^{\ \ 2}}{MKn} - \frac{T_{...}^{\ \ 2}}{MKLn} \quad dof_C = L-1$$

$$SS_{AB} = \sum_{i=1}^{M} \sum_{j=1}^{K} \frac{T_{ij..}^{\ \ 2}}{Ln} - \frac{T_{...}^{\ \ 2}}{MKLn} - SS_A - SS_B \quad dof_{AB} = (M-1)(K-1)$$

$$SS_{AC} = \sum_{i=1}^{M} \sum_{k=1}^{L} \frac{T_{i.k.}^{\ \ 2}}{Kn} - \frac{T_{...}^{\ \ 2}}{MKLn} - SS_A - SS_C \quad dof_{AC} = (M-1)(L-1)$$

$$SS_{BC} = \sum_{j=1}^{K} \sum_{k=1}^{L} \frac{T_{.kl.}^{\ \ 2}}{Mn} - \frac{T_{...}^{\ \ 2}}{MKLn} - SS_B - SS_C \quad dof_{BC} = (K-1)(L-1)$$

$$\begin{aligned} SS_{ABC} &= \sum_{i=1}^{M} \sum_{j=1}^{K} \sum_{k=1}^{L} \frac{T_{ijk.}^{\ \ 2}}{n} - \frac{T_{...}^{\ \ 2}}{MKLn} \\ &- SS_A - SS_B - SS_B \\ &- SS_{AB} - SS_{AC} - SS_{BC} \\ &dof_{ABC} = (M-1)(K-1)(L-1) \end{aligned}$$

Table A-2 ANOVA Table

Source	SS	dof	MS	F
A	SS_A	(M-1)	SS_A/(M-1)	MS_A/MS_H
B	SS_B	(K-1)	SS_B/(K-1)	MS_B/MS_H
C	SS_C	(L-1)	SS_C/(L-1)	MS_C/MS_H
AB	SS_{AB}	(M-1)(K-1)	SS_{AB}/(M-1)(K-1)	MS_{AB}/MS_H
AC	SS_{AC}	(M-1)(L-1)	SS_{AC}/(M-1)(L-1)	MS_{AC}/MS_H
BC	SS_{BC}	(K-1)(L-1)	SS_{BC}/(K-1)(L-1)	MS_{BC}/MS_H
ABC	SS_{ABC}	(M-1)(K-1)(L-1)	SS_{ABC}/(M-1)(K-1)(L-1)	MS_{ABC}/MS_H
Error	SS_H	MKL(n-1)	SS_H/MKL(n-1)	
Total	SS_T	MKLn-1		

Square of sums for error term is defined by

$$SS_{Error} = SS_T - (SS_A + SS_B + SS_C + ... + SS_{ABC})$$
$$dof_{Error} = MKL(n-1)$$

Which its value and degree of freedom is equal to the zero if experiments are not replicated. In such a case, parameter effects with lowest F values can be considered as error terms.

Sample calculations by using the data in
Hata! Yer işareti başvurusu geçersiz. summarizes the results that will be used in analysis of variance calculations.
Table A-1 is given as follows:

$$SS_{AB} = \frac{1.78^2 + 1.76^2 + 1.80^2 + 1.81^2}{2} - \frac{7.15^2}{8} - 0.000612 - 0.0000125 = 0.000113$$

$$SS_{AC} = \frac{1.67^2 + 1.87^2 + 1.74^2 + 1.87^2}{2} - \frac{7.15^2}{8} - 0.000612 - 0.013613 = 0.000612$$

$$SS_{BC} = \frac{1.71^2 + 1.87^2 + 1.70^2 + 1.87^2}{2} - \frac{7.15^2}{8} - 0.0000125 - 0.013613 = 0.0000125$$

$$\begin{aligned} SS_{ABC} = {} & \frac{0.84^2 + 0.94^2 + 0.87^2 + 0.93^2 + 0.83^2 + 0.93^2 + 0.87^2 + 0.94^2}{1} - \frac{7.5^2}{8} \\ & - 0.000612 - 0.0000125 - 0.013613 \\ & - 0.000113 - 0.000612 - 0.0000125 = 0.000012 \end{aligned}$$

$$\begin{aligned} SS_{Error} = {} & 0.014988 - (0.000612 + 0.0000125 + 0.013613 + 0.000113 + 0.000612 \\ & + 0.0000125 + 0.000012) = 0 \end{aligned}$$

As analysis of variance can not be performed without error term, three sources with smallest SS value which were, B, BC and ABC are moved to the error term.
ANOVA table of the results is given in Table A-3. It is seen that factor C has the greatest F value. This means that it is the most significant parameter.

Table A-3 Anova Table of the Results

Source	**SS**	**DOF**	**MS**	**F**
A	0.000612	1	0.000612	48.32
C	0.013613	1	0.013613	1074.71
AB	0.000113	1	0.000113	8.92
AC	0.000612	1	0.000612	48.32
Error	0.0000380	3	0.0000127	
Total	0.14988	7		

APPENDIX B

DAQ SOFTWARE BLOCK DIAGRAM

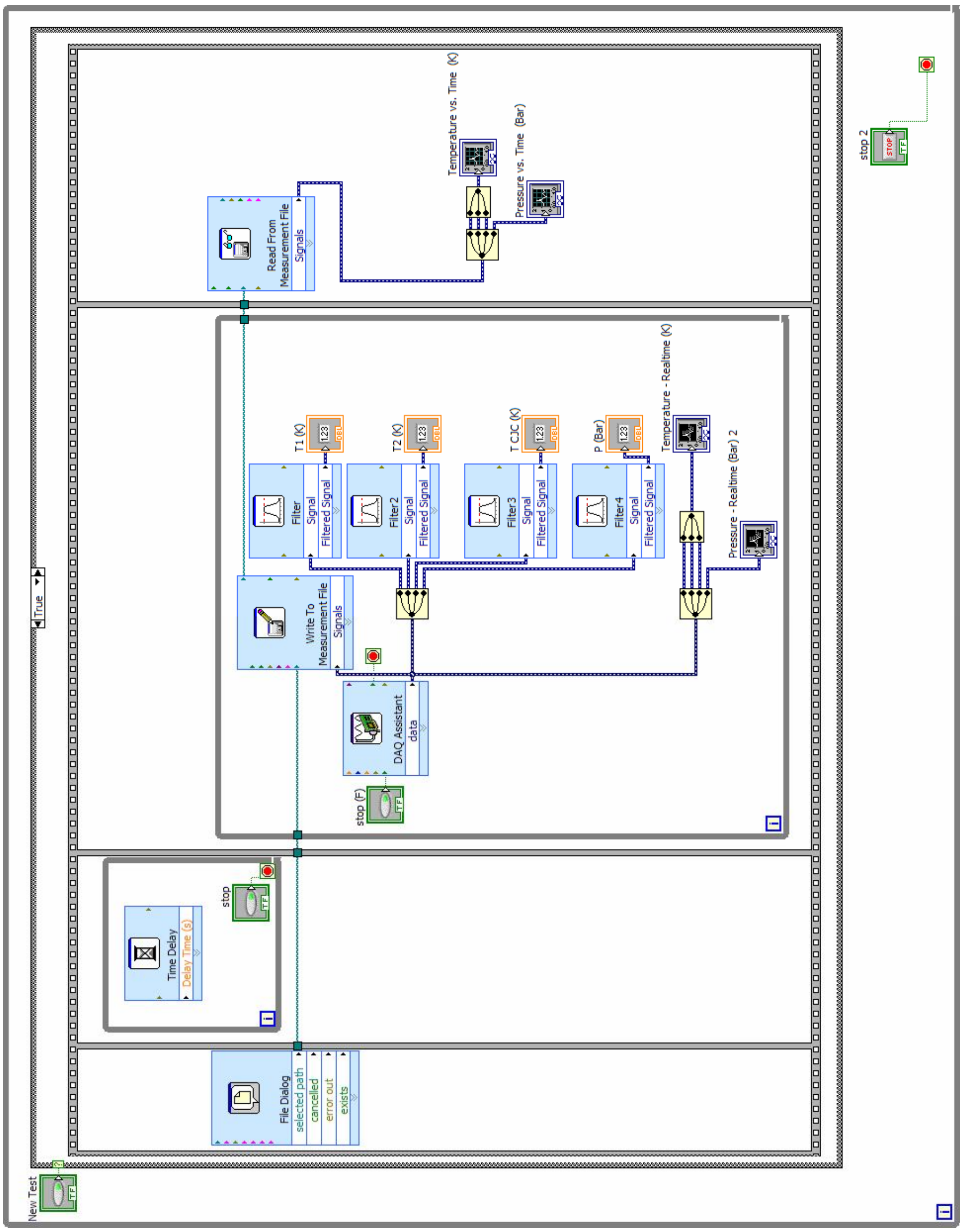

Figure B-1 DAQ Software Block Diagram